SANDIA REPORT

SAND2009-5904
Unlimited Release
Printed September 2009

Application of Advanced Laser Diagnostics to Hypersonic Wind Tunnels and Combustion Systems

Andrea G. Hsu, Jonathan H. Frank, Simon W. North

Prepared by
Sandia National Laboratories
Albuquerque, New Mexico 87185 and Livermore, California 94550

Sandia is a multiprogram laboratory operated by Sandia Corporation,
a Lockheed Martin Company, for the United States Department of Energy's
National Nuclear Security Administration under Contract DE-AC04-94AL85000.

Issued by Sandia National Laboratories, operated for the United States Department of Energy by Sandia Corporation.

Available to DOE and DOE contractors from
U.S. Department of Energy
Office of Scientific and Technical Information
P.O. Box 62
Oak Ridge, TN 37831

Telephone: (865) 576-8401
Facsimile: (865) 576-5728
E-Mail: reports@adonis.osti.gov
Online ordering: http://www.osti.gov/bridge

Available to the public from
U.S. Department of Commerce
National Technical Information Service
5285 Port Royal Rd.
Springfield, VA 22161

Telephone: (800) 553-6847
Facsimile: (703) 605-6900
E-Mail: orders@ntis.fedworld.gov
Online order: http://www.ntis.gov/help/ordermethods.asp?loc=7-4-0#online

SAND2009-5904
Unlimited Release
Printed September 2009

Application of Advanced Laser Diagnostics to Hypersonic Wind Tunnels and Combustion Systems

Andrea G. Hsu and Simon W. North
Department of Chemistry
Texas A&M University
P.O. BOX 3012
College Station, TX 77840

Jonathan H. Frank
Reacting Flows Department
Combustion Research Facility
Sandia National Laboratories
P.O. Box 969, MS9051
Livermore, CA 94551-0969

Abstract

This LDRD was a Sandia Fellowship that supported Andrea Hsu's PhD research at Texas A&M University and her work as a visitor at Sandia's Combustion Research Facility. The research project at Texas A&M University is concerned with the experimental characterization of hypersonic (Mach>5) flowfields using experimental diagnostics. This effort is part of a Multidisciplinary University Research Initiative (MURI) and is a collaboration between the Chemistry and Aerospace Engineering departments. Hypersonic flight conditions often lead to a non-thermochemical equilibrium (NTE) state of air, where the timescale of reaching a single (equilibrium) Boltzmann temperature is much longer than the timescale of the flow. Certain molecular modes, such as vibrational modes, may be much more excited than the translational or rotational modes of the molecule, leading to thermal-nonequilibrium. A nontrivial amount of energy is therefore contained within the vibrational mode, and this energy cascades into the flow as thermal energy, affecting flow properties through vibrational-vibrational (V-V) and vibrational-translational (V-T) energy exchanges between the flow species. The research is a fundamental experimental study of these NTE systems and involves the application of advanced laser and optical diagnostics towards hypersonic flowfields. The research is broken down into two main categories: the application and adaptation of existing laser and optical techniques towards characterization of NTE, and the development of new molecular tagging velocimetry techniques which have been demonstrated in an underexpanded jet flowfield, but may be

extended towards a variety of flowfields. In addition, Andrea's work at Sandia National Labs involved the application of advanced laser diagnostics to flames and turbulent non-reacting jets. These studies included quench-free planar laser-induced fluorescence measurements of nitric oxide (NO) and mixture fraction measurements via Rayleigh scattering.

ACKNOWLEDGMENTS

The authors wish to thank Dr. Rodney Bowersox for his guidance.

CONTENTS

FIGURES

TABLES

1. INTRODUCTION

1.1. Background and Motivation

The research project conducted at Texas A&M University is concerned with the experimental characterization and theoretical modeling of non-thermal and non-chemical equilibrium systems in hypersonic (Mach>5) shear layers using several experimental diagnostics. This effort is a Multidisciplinary University Research Initiative (MURI) and is a collaboration between the Chemistry and Aerospace Engineering departments. It is well known that hypersonic flight conditions can result in non-thermochemical equilibrium (NTE) state of air, where the timescale of reaching a single (equilibrium) Boltzmann temperature is much longer than the timescale of the flow. As air travels over a hypersonic vehicle and through shocks, the translational and rotational temperatures are excited rapidly to several thousands of degrees Kelvin, while the vibrational temperature lags behind. This trend is due to the fact that vibrational energy transfer requires orders of magnitude more collisions (typically 102 to 104) than translational or rotational energy transfers, which require on the order of 10-100 collisions. Therefore, behind the shock, the translational and rotational temperatures are much higher than the vibrational temperatures. As the three molecular modes equilibrate, the translational and rotational temperatures decay, while the vibrational temperature increases slightly. The equilibration timescale is on the same order as the convective timescale of the bulk flow.

The present studies investigate the transfer of energy from the vibrational mode to the translational and rotational modes. The NTE conditions have high vibrational temperatures (~2000K) with cold translational and rotational temperatures (~300K). During equilibration, the vibrational temperature decays, while the translational and rotational temperatures increase, which is opposite to what is encountered in true hypersonic flight as the air passes through a shock. The purpose of this experimental setup is twofold. First, it represents a real situation where the post-shock equilibrated air experiences an expansion, causing the vibrational temperature to freeze, and the rotational and translational temperatures to decay rapidly. Second, the research is a fundamental study of vibrational energy transfer and cascade, where the manner in which this energy cascade couples to flow properties is not well understood. In this research, we expect that only a small amount (typically on the order of a few percent) of the total molecules may exist in the excited vibrational states. However, the energetic spacing between vibrational levels is larger (by roughly an order of magnitude) compared to rotational spacing. A nontrivial amount of energy, about 10-20% of the total flow enthalpy, is therefore contained within the vibrational mode, and this energy cascades into the flow, affecting flow properties through the process of various vibrational-vibrational (V-V) and vibrational-translational (V-T) energy exchanges between the flow species. It is then useful to model the V-V and V-T energy exchanges to understand the mechanisms of the vibrational energy flow. In addition, chemical reactions may take place on the timescale of these energy transfer processes, such that the kinetics of these reactions must also be considered within the model. As a result, there has been increased interest in the characterization of non-thermal equilibrium systems [e.g., see Cheng (1995), Scalabrin (2005), Candler (1989), Osipov (2006), Roy (2006)].

At Texas A&M, the research is part of a larger effort in which the experimental data will serve as a benchmark to which fluid dynamics modeling, such as that discussed in Bowersox (2008), can be validated. The experimental research goals involve generation of the NTE encountered during hypersonic flight in a controlled environment within the laboratory using two methods: capacitively-coupled radio-frequency (CCRF) plasma discharge and laser photodissociation. In both cases, the NTE conditions cause the molecules to exist in a highly vibrationally excited state (thousands of degrees Kelvin), while maintaining "cold" (nearly room temperature, 300 + /- 10 to 30 K) rotational and translational temperatures (low temperature, low fluctuation). The NTE is then characterized using a suite of optical diagnostics. The research is broken down into two main categories: the application and adaptation of existing laser and optical techniques towards characterization of NTE, and the development of new techniques which have been demonstrated in an NTE flowfield, but may be extended towards a variety of flowfields. In Section 2, the experimental hardware and diagnostics system will be described. To understand the vibrational energy cascade in the post-CCRF flow, we include a brief section on vibrational kinetics modeling with comparisons to experimental N_2 CARS data. A computational study laying the groundwork for NO PLIF measurements in low temperature, low fluctuation flowfields such as those in the post-CCRF flow will be discussed with experimental validation. Section 3 will describe the application of molecular tagging velocimetry (MTV) techniques for one and two component velocity mapping in an underexpanded jet flowfield. Section 4 will describe NO quench-free PLIF and Rayleigh scattering measurements in towards combustion systems conducted at Sandia National Laboratories will also be discussed.

In summary, the research goals were: 1) generation of the NTE flowfield; 2) characterization of the NTE flowfield using laser and optical diagnostics; 3) development of software and image processing programs to acquire and analyze these data; 4) development of new molecular tagging laser diagnostic techniques for single component and two-component velocity mapping and application of laser diagnostic techniques towards combustion systems; 5) modeling and understanding of the chemical kinetic mechanisms for vibrational decay in both CCRF flowfield and NO_2 photodissociation studies 6) extension of laser diagnostics to research conducted at Sandia National Laboratories towards combustion flowfields.

2. EXPERIMENTAL HARDWARE AND FUNDAMENTAL STUDIES

2.1 Experimental Hardware

The experimental laser setup for the research at Texas A&M University consisted of a combination of a Spectraphysics PRO 290-10 Nd:YAG laser, two Spectraphysics LAB 150-10 Nd:YAG lasers, and two Sirah Cobrastretch tunable dye lasers. Additional hardware included a high-resolution 0.66 m, triple grating, SPEX spectrometer and an Oriel broadband spectrometer (MS125 1/8m with LineSpec CCD detector). The SPEX spectrometer was fitted with an electron-multiplying (EM) CCD (Andor, DU970N-BV). Two Andor iStar ICCD cameras (model DH734, 16-bit) fitted with Nikon 105mm F/4.0 UV lenses were used for imaging NO PLIF. The overall timing for the experiments was controlled by a digital delay generator (Berkeley Nucleonics Corporation, model DG565). A schematic of the laboratory layout is shown below:

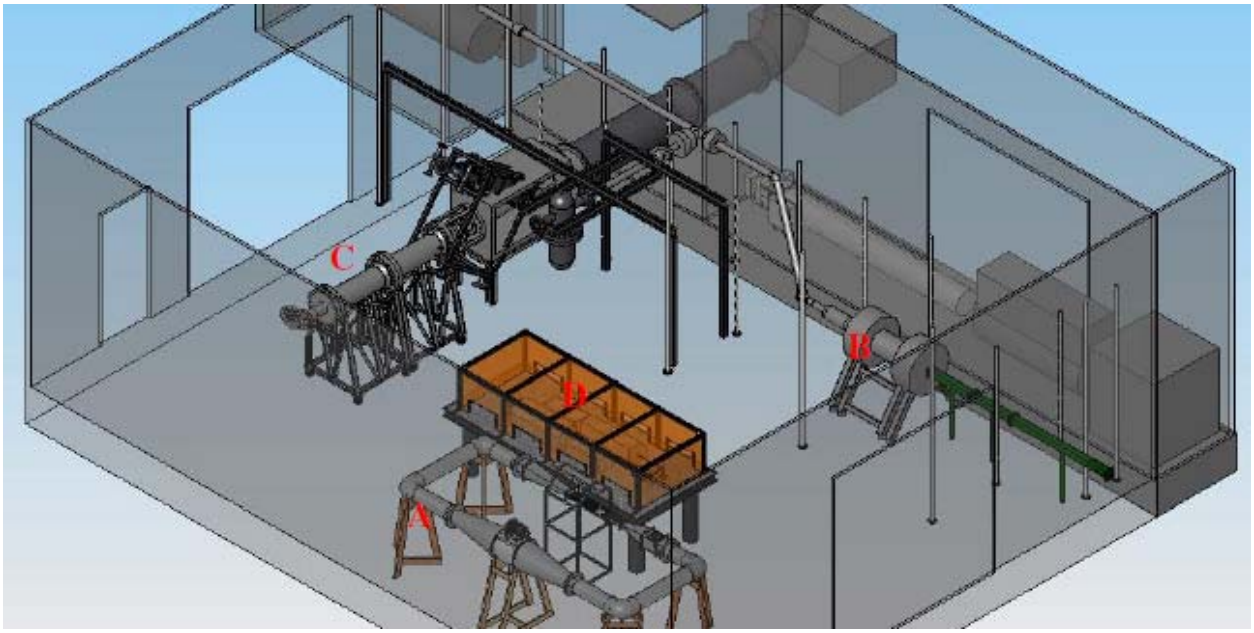

Fig. 1 National Aerothermochemistry Laboratory at Texas A&M University (schematic)

The diagnostic system is enclosed within the orange box situated in the center of the laboratory. The subsonic, supersonic, hypersonic facilities, and diagnostics center are labeled A, B, C, and D, respectively. The laser beams can be directed towards any of the flow facilities within the lab. Calibration measurements and the molecular tagging velocimetry studies were carried out in a portable vacuum chamber, shown below:

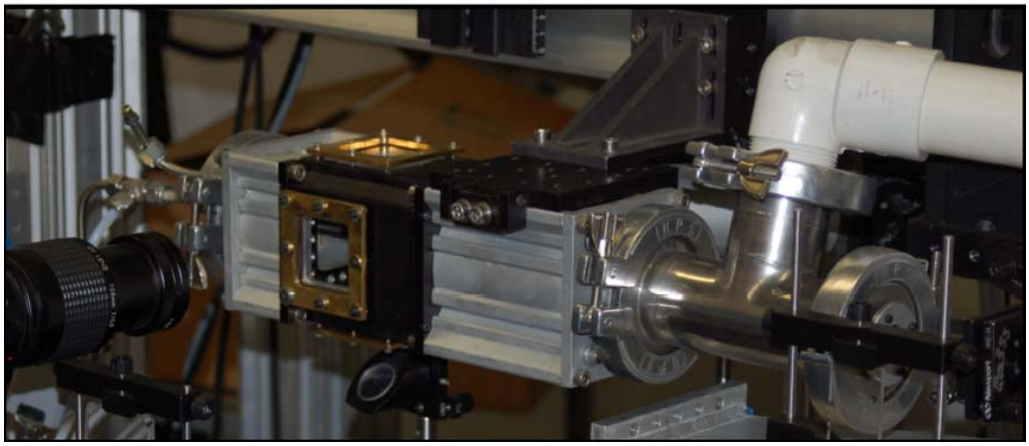

Fig. 2 Portable vacuum chamber (digital photo)

Lastly, attention was given to the subsonic test section, which was designed to generate the CCRF discharge. The subsonic test section was designed in Solidworks 2008. The following considerations were taken into account: 1) the area around the plasma section must be made of non-metallic materials; 2) optical access was required on 4 sides with flush mounted O-ring sealed fused silica windows (so as not to disturb the flow); 3) the test section must be able to be completely sealed for leak-testing; 4) the windows must be interchangeable incase of accidental breakage; 5) the entire top and bottom walls (including the area surrounding the electrodes) must be angled for a slight expansion down the length of the test section (~0.18°) to account for boundary layer growth (room for adjustment was preferable); and 6) the entire structure must be structurally rigid, especially since the test section would operate at ~20 Torr. This low pressure was required to maintain the CCRF discharge. In this design, all of the pieces were machined of aluminum except those in the vicinity of the plasma discharge region. The assembled test section is shown in Fig. 3 with a closeup of the plasma discharge section is shown in Fig. 4. This region was especially important and has several additional special design requirements: 1) the region around where the plasma is discharged must be made of non-metallic, dielectric, high-temperature resistant materials to prevent arcing and/or melting; 2) optical access must be available as close to the copper electrodes as possible on all four sides for plasma diagnostics; 3) the electrode tilt (pivot) must be adjustable to obtain an even plasma discharge across the width of the test section; 4) the Macor section must also expand out to relieve the growth of the boundary layer (~0.18°); and 5) the region must be leak-proof. Stress tests were conducted using Solidworks to assure that the structure would hold rigid under the vacuum loads.

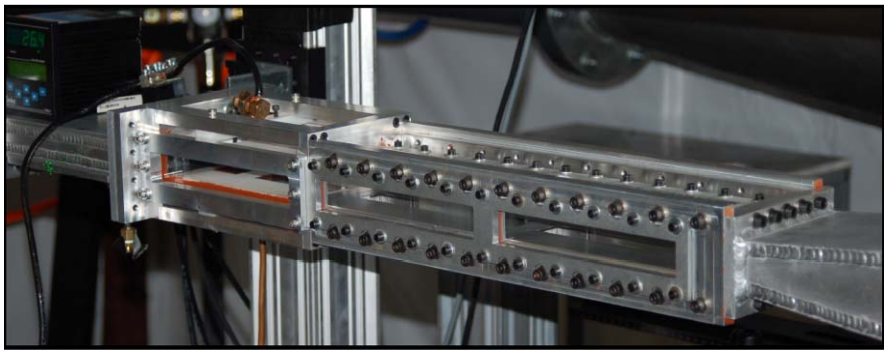

Fig. 3 Subsonic test section assembled

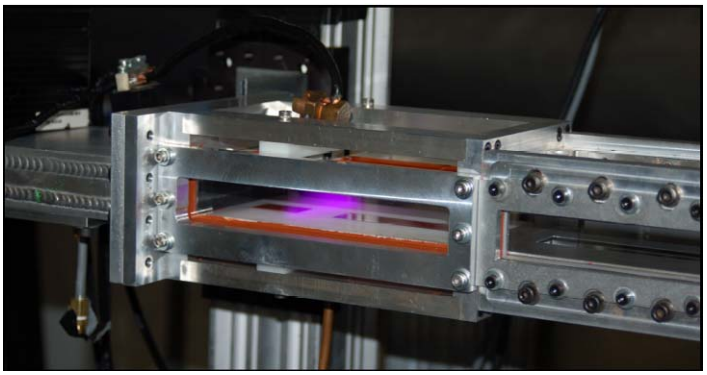

Fig. 4 CCRF plasma discharge in subsonic test section

2.2 Fundamental Studies

2.2.1. Fluorescence modeling using a multi-level model with comparison to experiment

The NO LIF measurements in this study were performed using transitions in the NO A-X (0,0) and (1,1) bands. The rotational lines within these bands were identified by comparing measured and simulated NO LIF excitation spectra. The simulated spectra were produced using LIFbase (Luque, 1999). In addition, fluorescence modeling was carried out using the 2-level model, which only accounted for a single ground and excited state, and a 5-level model which included rotational energy transfer in both the excited and ground states (Lee, 1993). A diagram of this model is shown below:

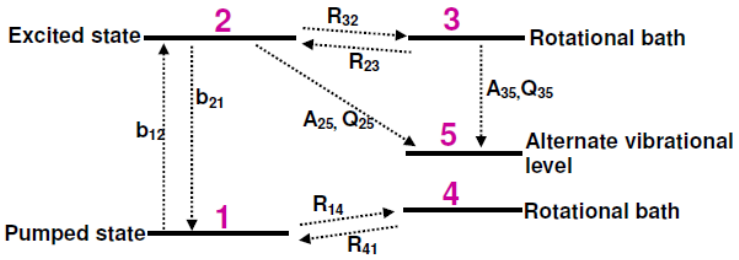

Fig. 5 Five-level model for NO fluorescence

These models were important in assessing the level of saturation expected. For sensitive rotational temperature measurements, it is important that the laser intensity was maintained in the linear fluorescence regime (unsaturated). This was verified experimentally by varying the laser intensity using a series of quartz plates, and observing the resulting NO fluorescence using both a photo-multiplier tube (PMT) and an ICCD camera from the calibration cell filled with a known concentration of NO. The calibration cell gas composition was typically 1% NO in Air or N_2, and the pressure was adjusted to match the pressure in the plasma test section (20-30 Torr) to account for pressure shifting. The experimental results were then compared to both the 5-level model and 2-level model, shown below. The simulations were conducted using Kintecus software written by Ianni (2008).

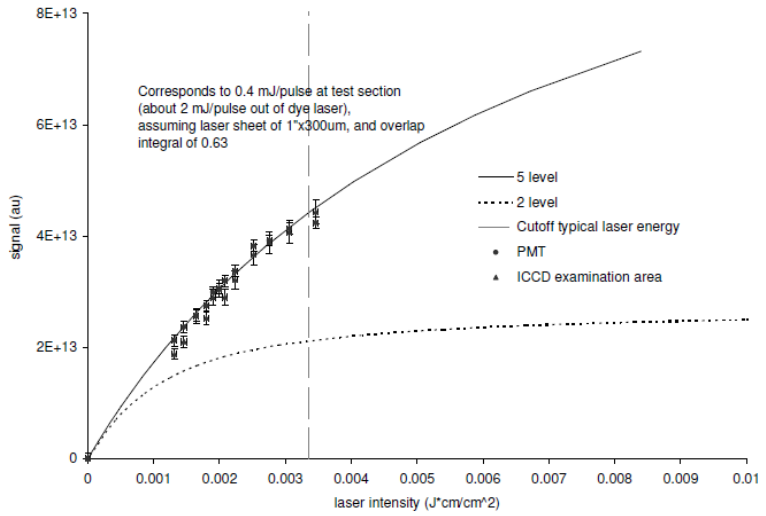

Fig. 6 PMT and ICCD fluorescence linearity comparison with modeling

As seen above, the LIF measurements probing the NO R1(3.5) rotational line follow the predictions of the 5-level model quite closely, demonstrating that rotational energy transfer is important in modeling NO fluorescence. Modeling the fluorescence with a 2-level model reduces the threshold of the onset of saturation, leading to an overly conservative estimate of onset of saturation. From these results, it was determined that the laser energy must be 0.4 mJ/pulse or less at the test section for accurate rotational temperature measurements.

2.2.2. Characterization of the CCRF discharge with comparison to vibrational kinetics modeling

A vibrational kinetics model was used to simulate the effect of the CCRF discharge on the gas flow. The model included the chemical species N_2, O_2, H_2O, CO_2, NO, and O. For N_2, O_2, and NO, only the ground state and first excited vibrational states were considered. In total, there were 104 reactions (52 forward and reverse pairs) accounting for the vibrational-translational (VT) and vibrational-vibrational (VV) energy transfers between the different species. The rate constants for many of the reactions have multiple values cited in the literature, and the most reliable (often the ones with the most experimental validation) were used in the model. The vibrational decay model is shown in Tables 1, 2, and 3 with associated references.

Table 1. Vibrational Translational (VT) energy exchanges considered for vibrational kinetics modeling

VT reaction	Forward rate constant	Ref.	Reverse rate constant	Ref.	Rxn #
$N_{2,v=1} + N_2 \Rightarrow N_2 + N_2$	4.13262×10^{-24}	Candler (2002)	5.2152×10^{-29}	DB	1
$N_{2,v=1} + O_2 \Rightarrow N_2 + O_2$	4.13262×10^{-24}	Candler (2002)	5.2152×10^{-29}	DB	2
$N_{2,v=1} + NO \Rightarrow N_2 + NO$	4.13262×10^{-24}	Candler (2002)	5.2152×10^{-29}	DB	3
$N_{2,v=1} + CO_2 \Rightarrow N_2 + CO_2$	5.2877×10^{-15}	Bass (1980)	6.67286×10^{-20}	DB	4
$N_{2,v=1} + H_2O \Rightarrow N_2 + H_2O$	5.2877×10^{-15}	Bass (1980)	6.67286×10^{-20}	DB	5
$N_{2,v=1} + O \Rightarrow N_2 + O$	3.5×10^{-15}	McNeal (1972)	4.41685×10^{-20}	DB	6
$O_{2,v=1} + O_2 \Rightarrow O_2 + O_2$	5.77103×10^{-19}	Bass (1980)	3.01357×10^{-22}	DB	7
$O_{2,v=1} + N_2 \Rightarrow O_2 + N_2$	5.58402×10^{-19}	Bass (1980)	2.91592×10^{-22}	DB	8
$O_{2,v=1} + NO \Rightarrow O_2 + NO$	6.54768×10^{-19}	Candler (2002)	3.41914×10^{-22}	DB	9
$O_{2,v=1} + CO_2 \Rightarrow O_2 + CO_2$	1.76896×10^{-20}	Bass (1980)	9.23734×10^{-24}	DB	10
$O_{2,v=1} + H_2O \Rightarrow O_2 + H_2O$	4.08765×10^{-15}	Bass (1980)	2.13453×10^{-18}	DB	11
$O_{2,v=1} + O \Rightarrow O_2 + O$	8.3×10^{-12}	Breen (1973)	4.33418×10^{-15}	DB	12
$NO_{v=1} + NO \Rightarrow NO + NO$	7.52×10^{-14}	Kosanetzky (1980)	8.33612×10^{-18}	DB	13
$NO_{v=1} + O_2 \Rightarrow NO + O_2$	2.58×10^{-14}	Kosanetzky (1980)	2.85908×10^{-18}	DB	14
$NO_{v=1} + N_2 \Rightarrow NO + N_2$	1.30×10^{-16}	Kosanetzky (1980)	1.44677×10^{-20}	DB	15
$NO_{v=1} + CO_2 \Rightarrow NO + CO_2$	7.14522×10^{-16}	Tsang (1986)	7.92276×10^{-20}	DB	16
$NO_{v=1} + H_2O \Rightarrow NO + H_2O$	1.8329×10^{-12}	Stephenson (1974)	2.03236×10^{-16}	DB	17
$NO_{v=1} + O \Rightarrow NO + O$	2.4×10^{-11}	Dodd (1999)	2.64847×10^{-15}	DB	18
$H_2O_{(010)} + H_2O \Rightarrow H_2O + H_2O$	5.50×10^{-11}	Finzi (1977)	2.67578×10^{-14}	DB	19
$H_2O_{(010)} + N_2 \Rightarrow H_2O + N_2$	4.99009×10^{-14}	Bass (1980)	2.42771×10^{-17}	DB	20
$H_2O_{(010)} + O_2 \Rightarrow H_2O + O_2$	4.99009×10^{-14}	Bass (1980)	2.42771×10^{-17}	DB	21
$H_2O_{(010)} + NO \Rightarrow H_2O + NO$	5.92126×10^{-14}	Palmer (1993)	2.88073×10^{-17}	DB	22
$H_2O_{(010)} + CO_2 \Rightarrow H_2O + CO_2$	no data		no data		23
$H_2O_{(010)} + O \Rightarrow H_2O + O$	no data		no data		24
$CO_{2,(001)} + CO_2 \Rightarrow CO_2 + CO_2$	6.81×10^{-15}	Huetz-Aubert (1971)	9.00134×10^{-20}	DB	25
$CO_{2,(010)} + CO_2 \Rightarrow CO_2 + CO_2$	5.24×10^{-15}	Bass (1980)	2.15724×10^{-16}	DB	26
$CO_{2,(001)} + N_2 \Rightarrow CO_2 + N_2$	1.85802×10^{-15}	Huetz-Aubert (1971)	2.45491×10^{-20}	DB	27
$CO_{2,(001)} + O_2 \Rightarrow CO_2 + O_2$	3.19348×10^{-15}	Cannemeyer (1973)	4.21938×10^{-20}	DB	28
$CO_{2,(010)} + N_2 \Rightarrow CO_2 + N_2$	3.16276×10^{-15}	Bass (1980)	1.30217×10^{-16}	DB	29
$CO_{2,(010)} + O_2 \Rightarrow CO_2 + O_2$	4.20879×10^{-15}	Bass (1980)	1.73284×10^{-16}	DB	30
$CO_{2,(001)} + NO \Rightarrow CO_2 + NO$	2.46976×10^{-14}	Bauer (1986)	3.38726×10^{-19}	DB	31
$CO_{2,(001)} + O \Rightarrow CO_2 + O$	1.9465×10^{-13}	Cramp (1973)	2.57181×10^{-18}	DB	32
$CO_{2,(001)} + H_2O \Rightarrow CO_2 + H_2O$	1.01586×10^{-12}	Bauer (1986)	1.39325×10^{-17}	DB	33
$CO_{2,(010)} + O \Rightarrow CO_2 + O$	3.00×10^{-12}	Castle (2004)	1.23516×10^{-13}	DB	34
$CO_{2,(010)} + H_2O \Rightarrow CO_2 + H_2O$	2.03×10^{-11}	Bass (1980)	8.35671×10^{-13}	DB	35

Note: DB refers to rate constants calculated via detailed balance, all rate constants are bimolecular rates

Table 2 Vibrational Vibrational (V-V) energy exchanges considered for vibrational kinetics modeling

VT reaction	Forward rate constant	Ref.	Reverse rate constant	Ref.	Rxn#
$N_{2,v=1} + O_2 \Rightarrow O_{2,v=1} + N_2$	7.58×10^{-18}	Bass (1980)	1.83067×10^{-19}	DB	36
$N_{2,v=1} + NO \Rightarrow NO_{v=1} + N_2$	1.04×10^{-15}	Candler (2002)	1.18432×10^{-16}	DB	37
$NO_{v=1} + O_2 \Rightarrow O_{2,v=1} + NO$	1×10^{-14}	Ree (1993)	2.1234×10^{-15}	DB	38
$N_2 + CO_{2,(001)} \Rightarrow N_{2,v=1} + CO_2$	5.11×10^{-13}	Bass (1980)	5.35359×10^{-13}	DB	39
$N_2 + H_2O_{(010)} \Rightarrow N_{2,v=1} + H_2O$	1.31×10^{-16}	Zuckerwar (1987)	5.04275×10^{-15}	DB	40
$O_{2,v=1} + CO_2 \Rightarrow O_2 + CO_{2,(010)}$	6.66×10^{-15}	Bass (1980)	8.4456×10^{-17}	DB	41
$O_{2,v=1} + H_2O \Rightarrow O_2 + H_2O_{(010)}$	2×10^{-12}	Joly (1977)	2.1467×10^{-12}	DB	42
$NO_{v=1} + CO_2 \Rightarrow NO + O_{2,(010)}$	no data		no data		43
$NO_{v=1} + H_2O \Rightarrow NO + H_2O_{(010)}$	1.1×10^{-12}	Palmer (1993)	2.50218×10^{-13}	DB	44
$CO_2 + H_2O_{(010)} \Rightarrow CO_{2,(010)} + H_2O$	no data		no data		45
$N_{2,v=1} + CO_2 \Rightarrow N_2 + CO_{2,(010)}$	3.27×10^{-15}	Zuckerwar(1987)	1.00232×10^{-18}	DB	46

Note: DB refers to rate constants calculated via detailed balance, all rate constants are bimolecular rates

Table 3 Chemical reactions considered for vibrational kinetics modeling

Chemical Reaction	Forward Rate constant	Ref.	Reverse rate constant	Ref.	Rxn#
$NO_{v=1} + NO_2 \Rightarrow NO + NO_2$	2.0000×10^{-12b}	Dodd (1999)	2.2000×10^{-16b}	DB	47
$O_2 + O \Rightarrow O_3$	5.9200×10^{-34c}	DeMore (1997)	4.3800×10^{-26b}	Heimerl (1979)	48
$NO + O \Rightarrow NO_2$	9.9925×10^{-32c}	Atkinson (2004)	1.0000×10^{-23a}	(estimated)	49
$O + O \Rightarrow O_2$	1.0500×10^{-33c}	Tsang (1986)	1.0000×10^{-94b}	Tsang (1986)	50
$O + NO_2 \Rightarrow NO_{v=1} + O_2$	9.5000×10^{-12b}	Dodd (1999)	no data		51
$2NO + O_2 \Rightarrow 2NO_2$	2.0000×10^{-38c}	Atkinson (2004)	2.9400×10^{-31b}	Tsang (1991)	52

Note: [a] unimolecular rate constant, [b] bimolecular rate constant, [c] termolecular rate constant

Six chemical reactions were considered, and included recombination reactions such as forming O_2, O_3, and NO_2 (amongst a few others). In addition, sensitivity analysis was conducted to assess the effect of humidity and CO_2. Although the mole fractions of these species may be small, they are significant because the vibrational relaxation of O_2, N_2, and NO with these molecules is rapid, and their presence must be taken into account in the vibrational kinetics decay modeling. The model was executed with initial vibrational temperatures for N_2, O_2, and NO of 1700K, 800K, and 2000K, respectively. These temperatures were calculated using electron cross sections gathered from the literature for plasma conditions similar to ours.

Without the presence of H_2O or CO_2, the calculated lifetimes of the vibrational temperature decay for N_2, O_2, and NO were 0.17 s, 0.13 s, and 350 μs, respectively. The very short lifetime of NO was mainly driven by the fast kinetics for V-V and V-T energy exchange. For example, the V-T energy exchange for NO with other species was 5 orders of magnitude faster than the V-T rates for O_2, and 10 orders of magnitude faster than those for N_2. Within the V-T rates for NO,

the exchange was much faster for NO with O_2 (2.58 x 10^{-14} cm^3/molecule/s) than with N_2 (1.30 x 10^{-16} cm^3/molecule/s). NO V-V rates showed a similar trend, with energy exchanges with O_2 about 2 orders of magnitude faster than with N_2. The lifetimes of O_2, and N_2 were both long compared to that of NO, with O_2 being slightly shorter (0.13 s) than N_2 (0.17 s). This trend resulted from the combined effect of faster V-T and V-V rates for O_2 as compared to N_2 with other species. V-T energy exchanges between O_2 and the main species of the flow (N_2, O_2, and NO) were all on the order of 10^{-19} cm^3/molecule/s (reactions #7-9), while the same exchanges for N_2 were extremely slow (reactions # 1-3). The forward rate of V-V transfer from N_2 to O_2 (reaction #36) was an order of magnitude faster than its reverse counterpart, which was due to the vibrational energy spacing differences. As a result, N_2 vibrational energy is rapidly transferred to O_2. The V-V exchange for O_2 with NO (reaction #38) was about 4 orders of magnitude faster than reaction #36. Consequently, O_2 dumps available vibrational energy into NO, which then very rapidly undergoes V-T energy exchanges and decays to the ground state. The resulting energy flow is a cascade from N_2 to O_2 followed by transfer to NO.

The chemical reactions played an insignificant role in the vibrational energy decay since there was no dissociation (formation of O atom) within the plasma and three body recombination of NO with O_2 to form NO_2 was extremely slow at 30 Torr. However, at higher pressures, reaction #52 could become important and reaction #47 may compete with V-V and V-T exchanges. In addition, the reverse of reaction #47, referred to as a chemical feed reaction in Dodd (1999), regenerates vibrationally excited NO, and would directly affect the vibrational decay of NO, as well as indirectly affect O_2 (and N_2 to a lesser degree).

The mechanisms through which H_2O and CO_2 impart their effects on the flow differ. The effect of H_2O is felt immediately by all species, mainly through its extremely fast V-T exchanges with the vibrationally excited diatomic species. The effect of CO_2, on the other hand, is felt through the fast V-V and V-T exchange with vibrationally excited N_2. Although V-V exchange rates for CO_2 with NO and O_2 are unavailable in the literature, they are thought to be slow compared to the energy exchange with N_2 since vibrationally excited N_2 and CO_2 (001) are very close energetically.

The RF plasma in the subsonic facility was characterized for the following properties: 1) species identification using broadband emission spectroscopy, 2) rotational and vibrational temperature (of the electronically excited states) of N_2 using narrowband emission spectroscopy, 3) vibrational temperature of the electronic ground state of N_2 using CARS with comparison to the vibrational kinetics modeling. The narrow emission spectra centered on the second positive emission bands of N_2 was fit with a theoretical spectra provided by DeJoseph (2008) and is shown below. Broadband emission spectra lacked any indications of dissociation. Therefore, the experimental emission data verified that the plasma imparted only slight gas heating (35 +/- 3 K) with negligible molecular dissociation.

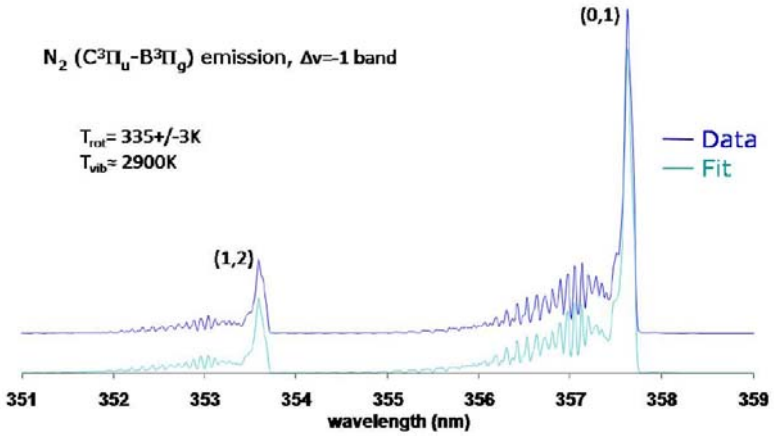

Fig. 7 Narrowband emission spectra of the N_2 second positive band

Emission data only provide the rotational and vibrational temperature of the electronically excited state (the N_2 C state, in this case). While the rotational temperature is representative of the bulk flow, vibrational temperatures in the electronically excited states are not easily coupled to the ground state and cannot be used to infer a ground state vibrational temperature. In addition, the vibrational temperatures for each of the chemical species may differ by several hundred degrees. N_2 CARS data was obtained by using a planar boxcars configuration at several locations downstream of the CCRF plasma. The N_2 vibrational temperature of the electronic ground state was calculated by fitting the measured CARS spectra to theoretical spectra produced with CARSFIT, a program developed at Sandia National Laboratories [Palmer (1989)] and provided by Roger Farrow (Sandia CRF). The simulated spectra used a rotational temperature of 335K, which was determined from the emission data. The fit of the experimental CARS data to the CARSFIT simulations was quite good. The vibrational temperature of N_2 as measured via CARS at a location of 1 in. downstream of the plasma was 1600K. The value within the plasma was expected to be slightly higher and close to 1700K, which was the value predicted via electron cross sections. For comparison, the vibrational temperature from the emission data, which directly measures the vibrational temperature of the N_2 C state, was approximately 2900K. Therefore, the vibrational temperature of the N_2 C state is clearly not equal to the vibrational temperature of the N_2 ground state. Continuing efforts are focused towards installation of a dual-pump CARS system to probe both N_2 and O_2 vibrational temperatures concurrently [Lucht (1987) and (2003)].

2.2.3. Development of software for processing NO PLIF data

As mentioned before, the plasma is expected to induce rotational and translational temperature fluctuations of +/- 35 K in a 300K flow. The goal is to detect these small fluctuations using NO PLIF, a challenging task; literature using NO PLIF for such high precision temperature measurements has not been found to date. In order to detect these extremely small fluctuations, the inherent noise on the fluorescence images must be suppressed. The most straightforward way to accomplish noise suppression is through Gaussian smoothing of the PLIF images. However, image smoothing reduces the spatial resolution of the measurements and must be used sparingly in order to avoid damping out true temperature fluctuations in the flow. Therefore, it becomes

challenging task to preserve the true and very small temperature fluctuations that occur in the flow while damping the noise in the images. The two main sources of noise are high-frequency noise (originating from shot, dark, and readout noise), and low-frequency noise (originating from laser beam profile inhomogeneity).

Computer simulations of the noise in the NO PLIF images were used to develop an image analysis scheme that minimized the effects of noise while preserving temperature fluctuation structures of a only few percent about the mean temperature. The computer based study was followed by experimental validation. Synthetic fluorescence images were generated using noise levels and dimensions of the experimental images. Typical "pockets" of temperature fluctuations were inserted into the images. The size of the largest structures was estimated to be about 1/8" according to the mesh size of the turbulence generating grid that was located upstream of the plasma. At a typical ICCD spatial resolution of 50-75 pixels/mm, this corresponds to 150-240 pixels. In order to resolve smaller turbulent structures, the size of the structures for the computer based experiment was set at 5 pixels (66 μm). The goal of the computer-based experiment was to test the synthetic images with a barrage of noise-suppression techniques to judge their effectiveness towards recovery of the true temperature map.

The rotational temperature is derived from taking the ratio of the two fluorescence images, where the images are obtained by probing two different rotational lines of NO. Then, the ratio of the images is related to the rotational temperature of NO (and subsequently the bulk flow since rotational energy exchange is rapid) via the Boltzmann equation:

$$R = \frac{S_{f2}}{S_{f1}} = C_{12} f_B, \text{ where } f_B = \left[e^{\frac{-\Delta E_{21vib}}{kT_{vib}}} \frac{(2J_2"+1)}{(2J_1"+1)} e^{\frac{-\Delta E_{21rot}}{kT_{rot}}} \right]$$

Where R is the ratio of fluorescence signals, S_{f2} and S_{f1}, at a particular pixel. C_{12} is a calibration constant, an F_B is the ratio of the Boltzmann populations of the probed states, and is a function of the energy differences between the probed states (ΔE), the degeneracy of the probed rotational states (2J+1 term), the Boltzmann constant, and the temperature (T). The vibrational temperature used for these experiments was 300K, since the vibrational temperature decay of NO was expected to be very fast downstream of the plasma. The vibrational kinetics model predicted that the temperature decayed to 300K within 1 in. of the plasma. This was verified experimentally by probing for vibrationally excited NO downstream of the plasma. The figure below shows a typical simulated NO PLIF image pair used for the computer based study:

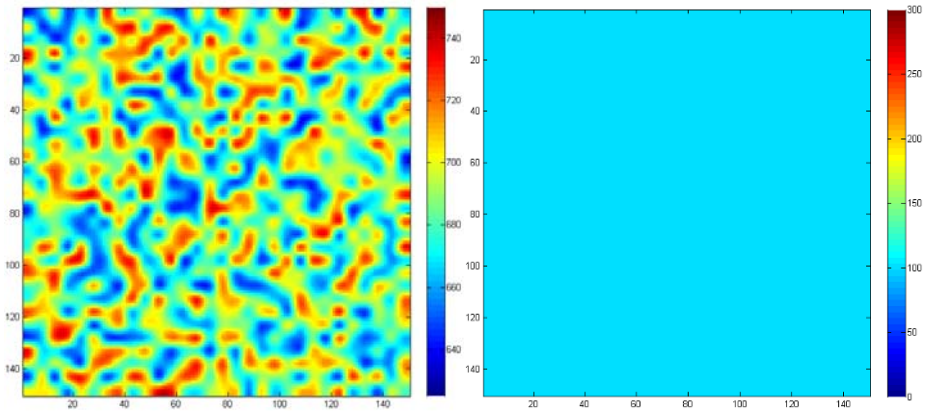

Fig. 8 NO fluorescence synthetic image generation

Notice that all the "temperature information" is contained in the image on the left. This assignment was arbitrary. The ratio of the two images was set to give a resulting temperature map with a mean temperature of 300 K, with temperature fluctuations of +/-10K. As previously mentioned, the size of the structures was set at 5 pixels and were randomly distributed throughout the image. The images were then masked with typical levels of high and low frequency noise. Figure 9 shows sample simulated NO PLIF images with added noise.

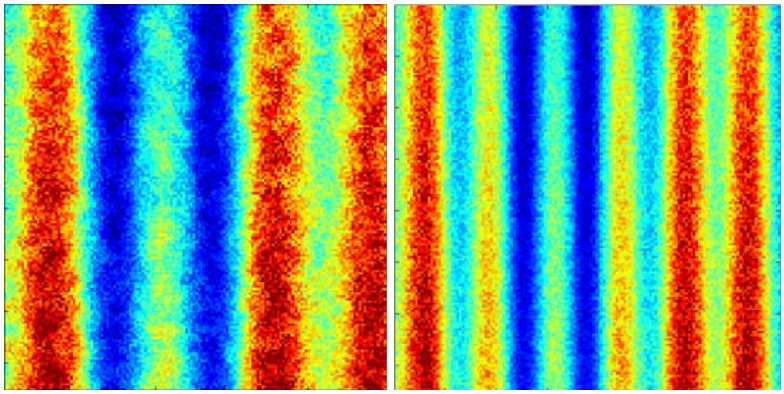

Fig. 9 NO fluorescence synthetic image generation after noise application

As can be seen from the image, these corrections nearly masked the original structure of the flow. The goal of the image analysis software experiment was to recover the true temperature map as accurately as possible through noise suppression techniques. The image pair was processed using a variety of commonly used corrective procedures. Exploration of how the following image processing procedures affected uncertainties of the resulting NO PLIF temperature map was conducted:

As can be seen from the images, the addition of noise masked the original structure of the flow. The goal of the image analysis was to recover the true temperature map as accurately as possible through noise suppression techniques. The image pair was processed using a variety of common corrective procedures. Exploration of how the following image processing procedures affected uncertainties of the resulting NO PLIF temperature map was conducted:

1. “Tightness” of the banding correction. In order to correct for the vertical banding in the images, the image was integrated in the vertical direction to obtain one banding function. This function was then smoothed by a running average of a number of pixels; this number of pixels was a variable in the analysis and is referred to as the “tightness” of the banding correction. The image was then normalized by dividing each row by the banding function.

2. Gaussian filtering of the images. This was the equivalent of applying a lowpass filter to the images. We explored Gaussian filters with a number of kernel sizes, as well as not filtering the images at all.

3. Choice of rotational lines. This choice is an important variable since choosing a pair of rotational lines with a larger energy difference decreases temperature uncertainties, but gives inherently noisier images due to lower population of the higher rotational line. This tradeoff was explained in detail in McMillin (1993). For this analysis, J=3.5 was maintained as the lower rotational lines, and the higher rotational lines was varied from J=5.5, 10.5, 14.5, 15.5, 16.5, and 19.5.

These corrections were applied, and the resulting T_{rms} was determined. T_{rms} refers to the uncertainty of the measurement, and was determined by subtracting the true temperature map from the derived map. The effects of banding tightness were intuitive; as the number of pixels in the smoothing kernel was increased, the amplitude of the banding function decreased, and the image was under corrected for the banding. This under correction caused inherent errors which were manifested in hot and cold bands (from 315 to 285K) in the temperature map. In fact, the temperature map is extremely sensitive to the banding function; a few percent errors (3-4%) in banding function correction cause the temperature to swing in the range of +/- 20K. The study on banding tightness showed that the smallest possible smoothing kernel should be used in order to fully capture the variations of the laser beam profile.

Gaussian smoothing significantly decreased the noise. Even minimal 2x2 and 3x3 smoothing (where 2x2 refers to the dimensions of the Gaussian kernel) decreased the uncertainties by factors of 2 and 3, respectively. The Gaussian smoothing was most beneficial where T_{rms} was lowest, and corresponded to a Gaussian kernel of 5-7 pixels point represented the optimal trade-off between uncertainties and resolution. At this point T_{rms} reached a very low <1%. At these measurement uncertainty levels, real temperature fluctuations on the order of 3% (300+/- 10 K) were easily distinguished. Generally, it was found that Gaussian smoothing with a kernel on the order of the structure size led to the lowest temperature uncertainties, known as the theory of matched filters. This theory was tested with a similar set of images with larger structure sizes (10 pixels instead of 5), and verified. Since the size of the smallest turbulent structures in the experiment was not known a-priori, the images were smoothed with a kernel that was equal to the width of the laser sheet. The spatial averaging within the image was thus comparable to the out-of-plane averaging. Using a razor blade and photodiode, we measured a laser sheet width of 150 μm, which corresponded to about 10 pixels on a full resolution image.

It was seen that T_{rms} decreased as the rotational energy spacing was increased, as expected. The higher rotational states that give an uncertainty of less than 2% include J=14.5, 15.5, 16.5, and 19.5. The NO LIF spectra simulated using LIFBASE showed that J=14.5 was somewhat close to

the R21 branch and was discarded as an option. From McMillin (1993), a good starting point is to begin with a pair of lines where the spacing is approximately equal to kT (208 cm^{-1}). However, past experiments using J=3.5 and 10.5 (ΔE=165 cm^{-1}) gave much too large temperature uncertainties of ~10%. Therefore, it was decided that J=3.5 and J=16.5, which gave T_{rms} of <2% and <1% at 2 and 5 pixel Gaussian smoothing, was an appropriate pair of lines to begin the NO PLIF temperature measurements.

The corrections mentioned in the above paragraphs were then implemented into a MATLAB-based GUI software. To test the validity of the image processing software in producing acceptable levels of temperature uncertainty, experiments were conducted in a slow uniform, 300K, air flow with seeded 1% NO. 280 images were acquired; a typical experimental fluorescence image pair is shown below:

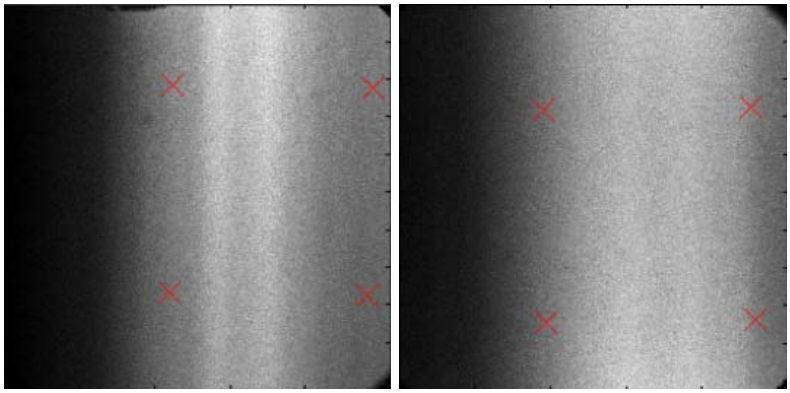

Fig. 10 Experimental NO fluorescence image pair probing J=3.5 (left) and J=16.5 (right)

The images were warped to equivalent fields of view via a dotcard, the corners of which are denoted by red crosses. The images were then processed, and the resulting mean temperature and T_{rms} maps are shown:

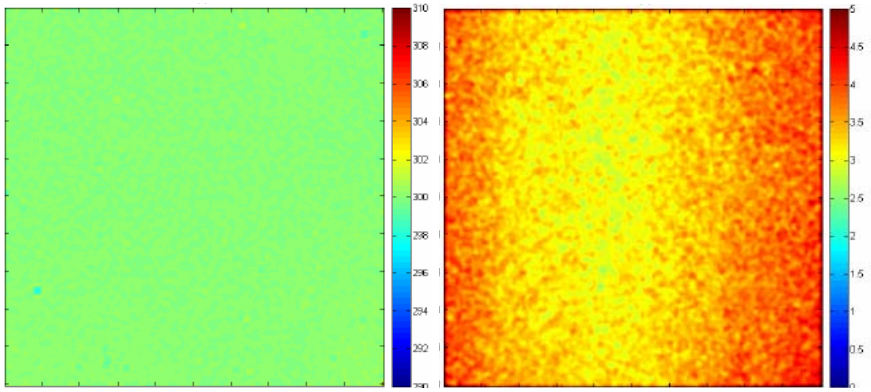

Fig. 11 Experimental mean temperature (left) and T_{rms} (right) maps

The plot of T showed a very uniform, 300K map, as expected. The T_{rms} map showed that the image processing was successful in producing measurement uncertainties of <5K, or <2%. In addition, the uncertainties reflected the laser energy distribution; uncertainties were lowest

(<1%) in areas of maximum laser energy, and greatest (~1.5%) near the edges of the field of view (where the laser energy decreased to about 2/3 of the maximum energy).

In summary, the application of PLIF towards flowfields with temperature fluctuations of a few percent (300 +/- 10K) was explored. The effects of banding tightness for beam-profile corrections, Gaussian smoothing for noise reduction, and rotational line pair selection were explored via computer simulations. It was concluded that a small banding tightness value, combined with Gaussian smoothing with a kernel on the order of the size of temperature fluctuation structures, and a rotational line pair selection of J"=3.5 and 16.5 were appropriate starting conditions. These conditions were applied towards an experimental, uniform air flow seeded with 1% NO. Resulting measurements of T and T_{rms} supported the image processing conclusions and gave T_{rms} <1.5%, or T_{rms} <5K, making resolution of true temperature of 300 +/- 10K (or greater) possible.

3. UTILIZATION OF NO_2 PHOTODISSOCIATION FOR ONE AND TWO COMPONENT VELOCITY MAPPING

3.1 Single Component Molecular Tagging Velocimetry

Molecular tagging velocimetry (MTV) measurements were performed by tracking the movement of NO molecules in time with NO PLIF imaging. The technique was demonstrated in an underexpanded jet, which is a well-known flowfield, and whose velocity fields can be simulated via CFD for comparison to experiment. The NO molecules were generated by photodissociating NO_2, which was seeded into the flow. The photodissociation of NO_2 at 355 nm produces both ground and excited vibrational states of NO. The ratio of the population of the nascent NO in the ground state to the vibrationally excited NO, $NO_{v=0}$:$NO_{v=1}$ has been experimentally determined to be 60:40 [e.g., see Hunter (1993), Brookes (2007), Harrison (1994)]. In the single component MTV study, the flowfield was interrogated by "writing" a line of NO with a photodissociation laser beam (355 nm), and the location of the NO was probed at two times (Δt = 400 ns) using two laser sheets that excited LIF in the NO gamma band. The streamwise velocity was determined by measuring the displacement of the photodissociation line and dividing by the time delay between the two NO PLIF measurements. The photodissociation beam was translated to 16 locations to measure the streamwise velocity across the entire flowfield.

To determine the optimal NO LIF excitation scheme, we compared the signal-to-noise ratios of NO LIF measurements using excitation of transitions in the NO (1,1) band near 224 nm and the (0,0) band at 226 nm. In the $A^2\sum^+_{1/2}(v'=1) \leftarrow X^2\prod_{1/2}(v''=1)$ band, the rotational states probed for the first and second probe lasers were R_1+Q_{21}(1.5) and the group of lines at the bandhead surrounding Q_1 (1.5), respectively. The experiment was then repeated, except $NO_{v=0}$ was probed instead of $NO_{v=1}$. Both lasers probed the R_1+Q_{21}(2.5) rotational states in the $A^2\sum^+_{1/2}(v'=0) \leftarrow X^2\prod_{1/2}(v''=0)$ band.

Our experiments emulated flow systems with naturally occurring NO, such as a combustion flowfield, by seeding NO into the flow. The naturally occurring NO produces a background LIF signal that must be distinguished from that of the photolytically produced NO. The flowfield that was examined for demonstration of the velocity mapping was the axially symmetric highly underexpanded jet. The terminology that will be used in this study was referenced from Woodmansee (2004). The structure of the highly underexpanded jet is well known [e.g., see Donaldson (1971)]. Typical images resulting from photodissociation of seeded NO_2 and subsequent probing of the NO (1,1) band (left) and the NO (0,0) band (right) are shown below at several photodissociation locations.

.

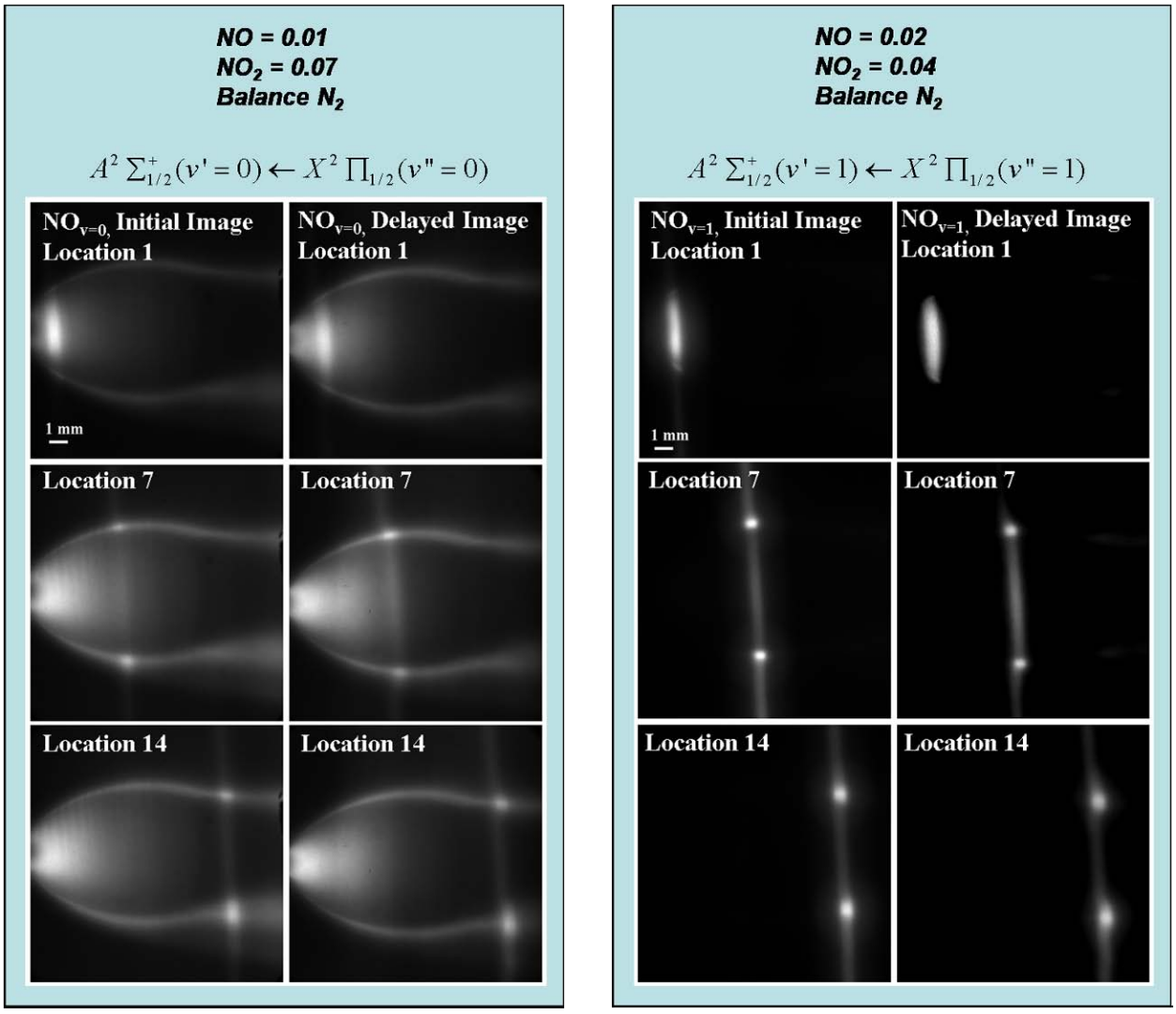

Fig. 12 NO fluorescence images resulting from probing NO (1,1) (left) and NO (0,0) (right)

Simply from visual assessment of the raw images, it is clear that the images probing NO (0,0) suffer from background NO fluorescence. The photodissociated NO is clear in both cases, although the NO (1,1) excitation provides much larger contrast and hence better signal to noise. The resulting compiled streamwise velocity map from the NO (1,1) images is shown below:

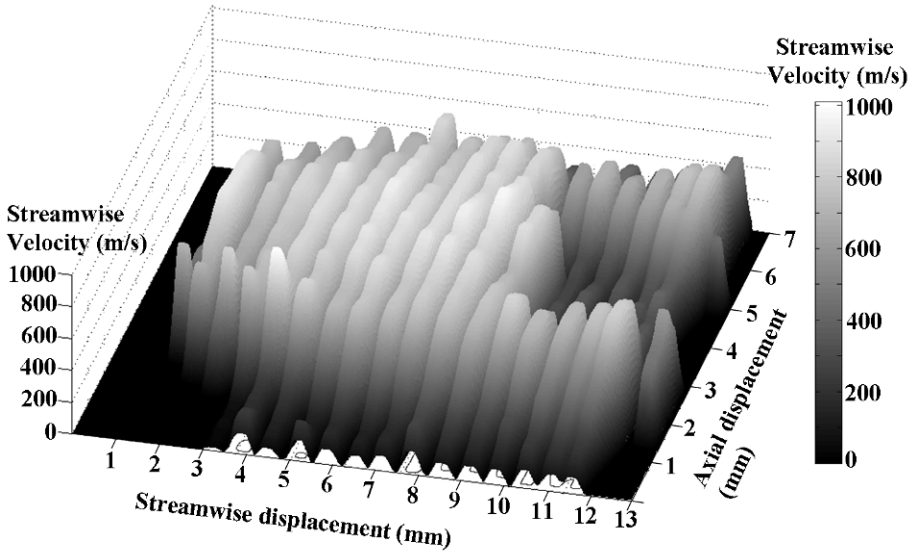

Fig. 13 Single component (streamwise) velocity map

The photodissociation of NO_2 at 355 nm produces a spatially localized non-thermal (NO $T_{vib} \approx$ 7000K) equilibrium population distribution of NO, and the NO T_{vib} decay can be temporally tracked via the Boltzmann relation. Although the rotational and vibrational temperatures differ in this non-thermal equilibrium system, the populations within the rotational and vibrational manifolds are distributed according to a Boltzmann distribution. Therefore, each manifold can be described by a Boltzmann temperature. Examples of such non-thermal equilibrium flows include plasmas and hypersonic re-entry. This experiment requires that the (1,1) and (0,0) transitions from a single photodissociation event are probed nearly simultaneously. The images are taken at a given time (in steps of μs) after the photodissociation event and are then ratioed on a pixel-by-pixel basis in a manner analogous to that used in the calculation of rotational temperature. The resulting image is a map of the NO $T_{vib.}$ A series of images were taken at different times after photodissociation and the centerline vibrational temperatures were compared to kinetics simulations with excellent agreement. The model was sensitive to the quenching of vibrationally excited NO by O atom formed through the photodissociation of NO_2. However, even with the effect of O atom quenching, $NO_{v=1}$ existed in moderate quantities for tens of μs. The effects of thermal decomposition of NO_2 (relevant to combustion flowfields) and diffusion were examined. Single shot image analysis yielded streamwise velocity (1σ) uncertainties of 5%.

3.2 Two Component Molecular Tagging Velocimetry

As discussed in the previous section, MTV has been applied using both single-line and grid techniques. The single-line techniques provide only one component of velocity, while the grid techniques give two components of velocity in the laser plane by observing the warping of the grid, i.e. the movement of the intersection points of the grid. Gaseous grid studies for two-component velocimetry are exceedingly rare in the literature and limited to only a few studies using biacetyl [Ismailov (2006), Stier (1999)] and OH [Ribarov (2004). The present experiment examines the application of MTV towards two-component velocimetry in a variety of quenching

environments and compares the advantages and disadvantages of the MTV techniques. The technique relies on the formation of two co-planar, perpendicular laser sheets into a grid, and the tracking of the grid via imaging onto ICCD detectors. The velocity is determined by calculating the displacements of the grid intersection points and dividing these values by the time delay between the two images. Two types of MTV will be explored. The first approach, referred to as the fluorescence lifetime technique, uses LIF detection of NO that is seeded into the flow. Both the initial and time delayed images are recorded during a single fluorescence lifetime using a two-laser, two camera setup. The two lasers are pulsed simultaneously to increase the signal-to-noise ratio of the NO LIF measurements. The ability to detect the fluorescence signal in the time-delayed image depends on the fluorescence lifetime, which is a function of the local quenching rate. In the second MTV approach, referred to as the photodissociation technique, NO is produced by photodissociation of seeded NO_2, which is then probed using two temporally separated lasers for the initial and time delayed LIF measurements. This approach requires a three-laser, two camera setup. Since two separate probe lasers are used, there was no concern of fluorescence lifetime and thus this technique should be less susceptible to quenching effects. The advantages of the two MTV approaches in different quenching environments will be examined. The study represents the first known application of molecular tagging velocimetry utilizing either the fluorescence lifetime or photodissociation technique towards two-component velocity mapping. Three quenching conditions were run with the two MTV techniques: 1) Low quenching, fluorescence lifetime, 2) High quenching, fluorescence lifetime, and 3) High quenching, photodissociation. The resulting images from the three conditions are shown below. The first, second, and third conditions are shown in the left, middle, and right panels, respectively. The raw (grayscale) images are shown, where the time delay between the two images used for the velocimetry analysis was 400 ns. The resulting calculated two-component velocity maps are shown below the grayscale images and are deconstructed into streamwise and radial component maps.

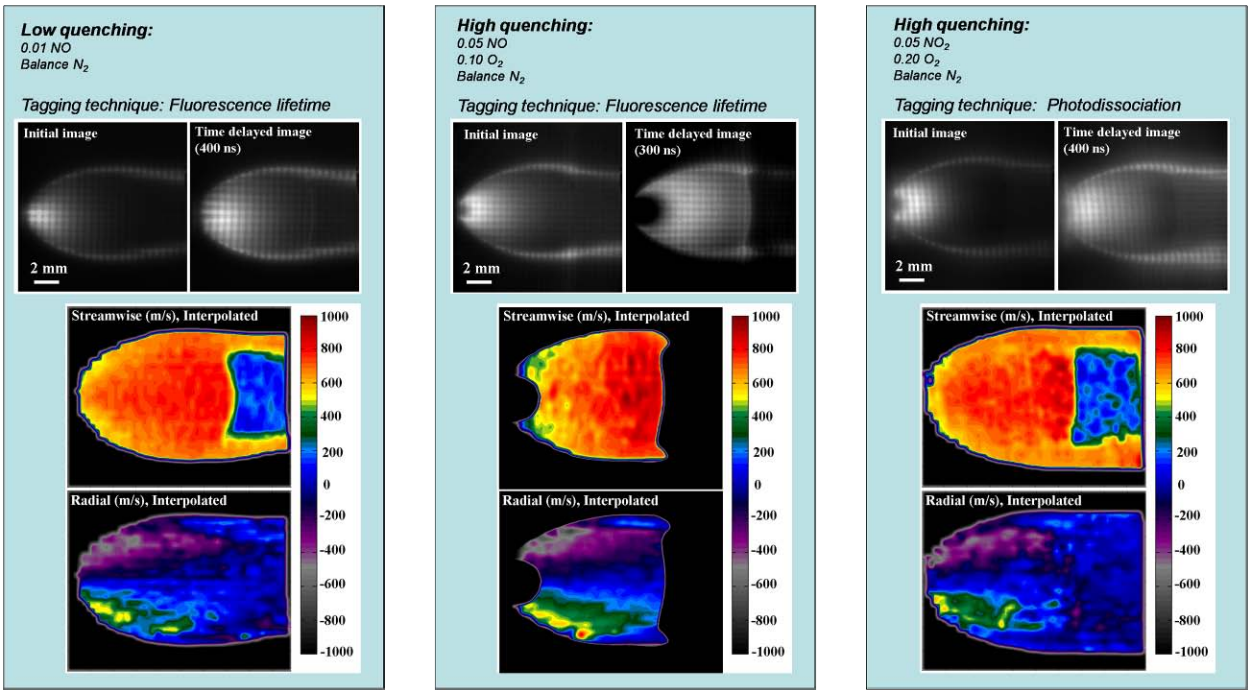

Fig. 14 Two-component velocity mapping results in varying quenching conditions

From these data, the following conclusions were drawn:

1) In low-quenching, high-speed flows, the fluorescence lifetime technique yields excellent recovery of velocity vectors in all areas of the flow (left panel).
2) In high-quenching conditions where the fluorescence lifetime is shortened, and particularly in low-speed flows, this technique is limited (middle panel) resulting in lost velocity vectors near the nozzle and in the subsonic area following the Mach disk
3) Use of the NO_2 photodissociation technique circumvents the quenching problem via the long lifetime of the NO photoproduct (tens of μs), and may be used in high-quenching and either low or high speed flows (right panel).

The two-component technique produced velocity maps which matched CFD simulation results, as shown below:

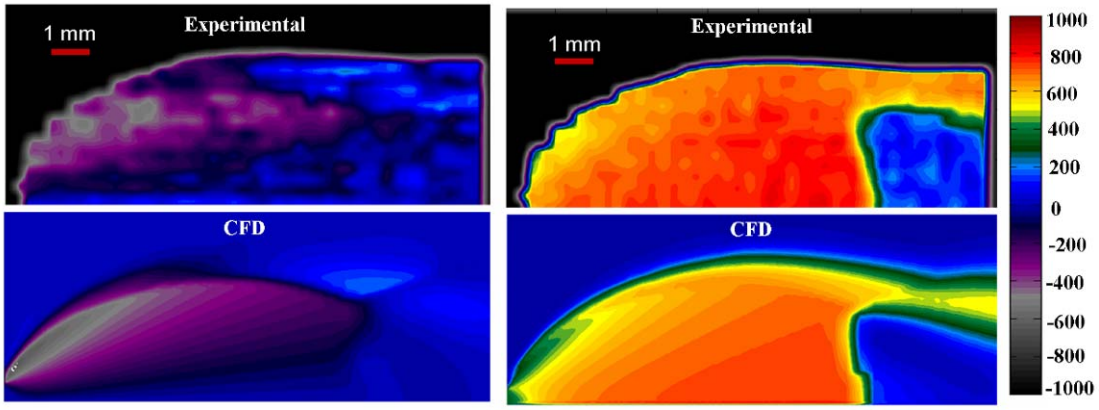

Fig. 15 Comparison of experimental two-component velocity maps to CFD

The streamwise and radial velocity maps had a maximum spatial resolution of 1 velocity vector per 270 um x 270 um. Typical resolutions were approximately 1 velocity vector per 400 um x 400 um. Resolution was limited by the amount of smoothing applied to the raw images, which was directly limited by the signal to noise ratios of the NO LIF measurements. Single shot analyses of the photodissociation technique yielded relative uncertainties of ~5% and were primarily limited by signal to noise. Large fluctuations in the vicinity of the Mach disk were due to shot-to-shot fluctuations in the location of the Mach disk and were inherent to the nature of the flow. Since the calculated NO_2 photodissociation fraction was greater than 99.9%, the uncertainties could be improved by either increasing NO_2 number density (followed by a subsequent increase in photodissociation laser intensity), or by increasing probe laser energy. One way to increase velocity resolution (and also decrease uncertainties) which would have an especially large effect in the subsonic region would be the adaptation of the velocimetry code to give sub-pixel resolution.

4. QUENCH-FREE NO LIF MEASUREMENTS AND LASER RAYLEIGH SCATTERING MEASUREMENTS AT SANDIA'S CRF

4.1 Quench - Free NO LIF Imaging

Laser-induced fluorescence is an extremely powerful and widely used diagnostic technique. However, collisional quenching complicates the conversion of laser-induced fluorescence signals to species concentrations because the quenching rate varies with the local temperature and composition. The idea of this diagnostic technique is to perform laser-induced fluorescence measurements on a timescale that is shorter than, or comparable to, the time between molecular collisions and thus eliminate the effects of collisional quenching. For gas-phase flows at atmospheric pressure, this technique requires sub-nanosecond laser pulses and detector gating. A picosecond distributed feedback dye laser is used for LIF excitation, and a fast-gated intensified CCD camera is used for detection.

Research conducted at Sandia National Labs' CRF in June of 2007 with Jonathan Frank, Ron Sigurdsson, and Carl Hayden involved the characterization of a fast-gated ICCD camera (LaVision Picostar), and the application of this camera towards quench-free NO PLIF measurements. The fast gating of this camera enables detection of the initial fluorescence signal, before the effect of quenching was manifested. The use of a shorter intensifier gatewidth reduces the effects of quenching, albeit with less signal. It is therefore important to measure the width of the intensifier gate and the dependence of the intensifier's throughput with gatewidth. The intensifier gatewidth was measured by illuminating the photocathode with 100 fs pulses from a doubled Ti:Sapphire laser and stepping the time delay between the laser pulses and the intensifier gating. At each time delay, the signal was averaged over multiple laser pulses and recorded. The mean signal over the central region of the intensifier is shown in Fig. 16 as a function of the time delay between the laser and intensifier gate.

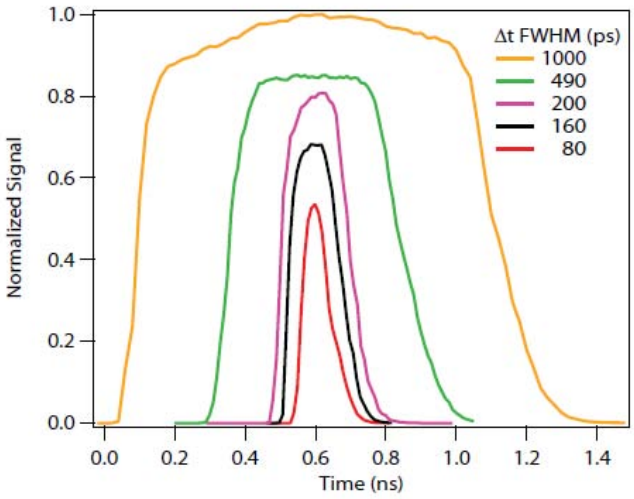

Fig. 16 LaVision Picostar intensifier gatewidths measured using ~100 fs pulses (doubled Ti:Sapphire laser)

The intensifier gatewidth measurements indicate that at longer gating times (1000 ps or greater), the shape of the gate is nearly square, as expected. However, as the gating times decreased, the gate became less ideal. In addition, the peak signal decreased as the gating time was decreased. For an 80 ps gatewidth, the peak intensifier throughput was reduced by approximately 50%.

The quench-free technique was demonstrated using NO LIF measurements in a two-channel flow with each channel having a different quenching environment. The experimental configuration is shown in Fig. 17. Oxygen is an efficient quencher of NO fluorescence, and the quenching rates of the two channels were set by using different concentrations of O_2 and N_2 as buffer gases. The buffer gas in each channel was seeded with 20 ppm of NO. A distributed feedback dye laser (~100 ps pulses, 0.8 mJ/pulse at 10 Hz) was used to probe the A-X(0,0) band of NO at 226 nm. The decay times of the NO LIF signals were measured using an MCP photomultiplier tube and a digital oscilloscope with 6 GHz bandwidth. The NO fluorescence lifetimes in the two channels were 1.2 ns and 4.3 ns. These measurements were performed in collaboration with T. Settersten (Sandia). An example NO fluorescence image of the two-channel flow is shown in Fig. 18 where the channels on the left and right represent the low and high quenching conditions, respectively. The normalized LIF signal is shown below the fluorescence image for different intensifier gatewidths. For a 3 ns gatewidth, the LIF signals in the two channels differed by approximately 50%. As the intensifier gate was decreased, the discrepancy between the fluorescence signal in the low and high quenching channels was reduced, indicating the decreased effect of quenching. For a 200 ps gatewidth, the LIF signals in the two channels differed by only 18%. These results demonstrate the effectiveness of this technique for reducing the impact of collisional quenching on LIF measurements. This approach is particularly valuable for flows with large variations in quenching rates, such as flames.

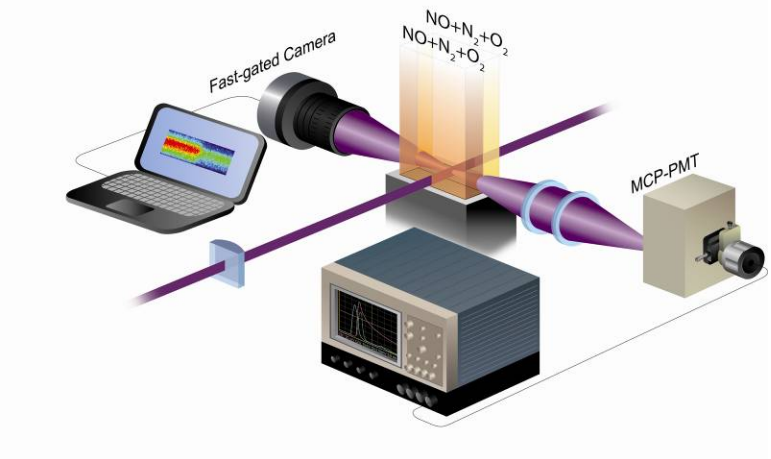

Fig. 17 Experimental configuration for quench-free NO LIF imaging

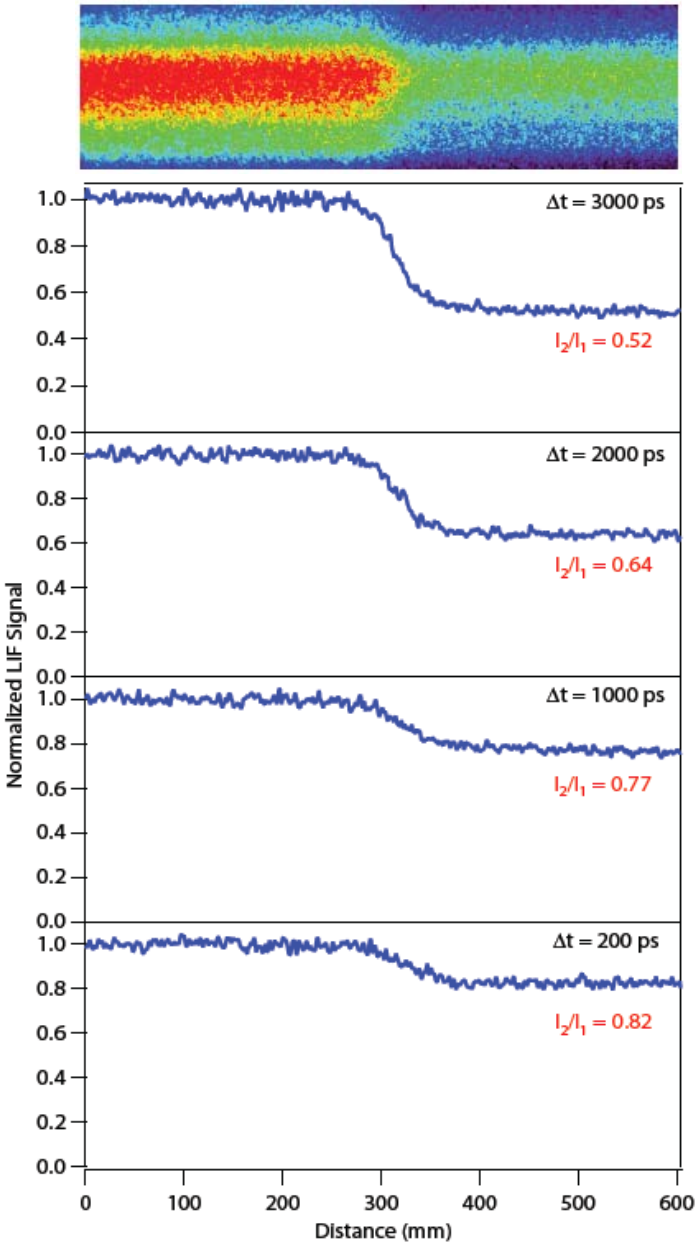

Fig. 18 Two-channel NO LIF images in different quenching conditions

4.2 Laser Rayleigh Scattering Measurements in Turbulent Jets

In the summer of 2008, measurements of dissipative structures in turbulent non-reacting jets were performed at Sandia's CRF with Jonathan Frank. This work was motivated by previous studies at Sandia on dissipative structures in both jet flames and non-reacting jets. Two of the goals of this research effort are to understand the effects of heat release on turbulence and to provide experimental data sets for developing accurate large eddy simulations (LES) in collaboration with Joseph Oefelein (Sandia). The new set of experiments extended previous measurements to higher Reynolds number jet flows. The results will be used to understand the

dependence of turbulence structures on Reynolds number and to investigate whether the fidelity of LES improves with increasing Reynolds number. In LES calculations, there is a fundamental assumption of scale separation for the energy and dissipation spectra. The small scales on which mixing takes place are assumed to be independent of the large scale turbulent motions. However, this assumption is not valid at low Reynolds numbers and may not be applicable to many laboratory scale turbulent flows and flames.

Highly resolved laser Rayleigh imaging was used to measure the fine-scale turbulence structures in a non-reacting propane jet issuing into ambient air. Previous measurements of similar jet flows were performed at Reynolds numbers of 22,000 and below, and the new measurements investigated Reynolds numbers of > 90,000. Challenges of the flowfield included resolution and reduction of noise requirements for detecting small turbulent structures, filtration of particles/droplets out of the flowfield, and pressure/flow limitations for achieving high Reynolds numbers. The turbulent non-reacting propane jet issued into air from an 8 mm diameter nozzle with a tapered edge. A frequency doubled Nd:YAG laser (~800 mJ/pulse at 532 nm) was used to excite Rayleigh scattering, and the resulting scatter was captured onto a CCD camera (Cooke, Inc.). A beam profiling camera (Cooke, Inc) was used to correct the images for shot-to-shot variations in the laser beam profile. Two parallel mass flow controllers (500 slm each, MKS) were used to increase the available mass flow rate of propane, and multiple filters were used to reduce particles in the flow. Images were collected at 3 downstream locations (x/d of 2, 10, and 20), shown below (left panel). The locations of the measurements are shown overlaid on an image of the jet flame for visual reference. Sample shots of the Rayleigh scattering images from the non-reacting jet at Re = 90,000 and Re = 22,000 (previous measurements) are shown in the top right and bottom right panels:

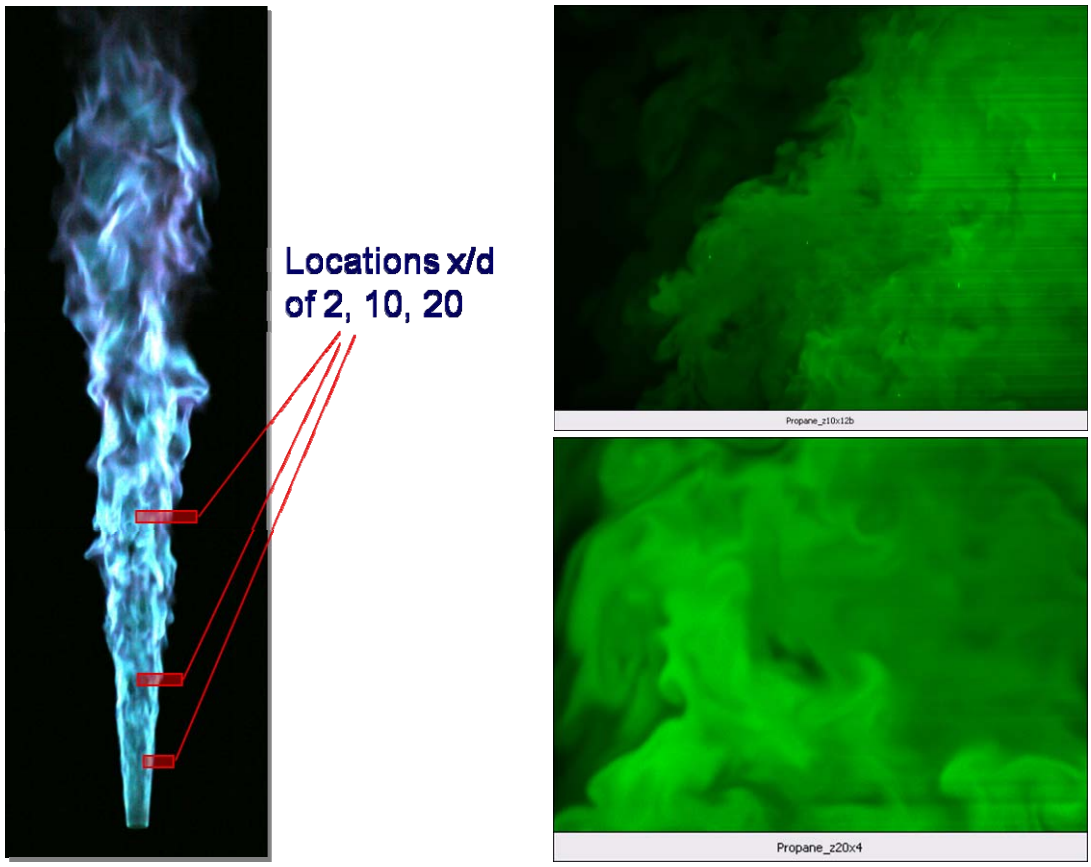

Fig. 19 Turbulent jet (left) and sample images at Re=90,000 (top right) and Re = 22,000 (bottom right)

As seen from the images, the higher Re results in smaller turbulent structures, many of which occur near the resolution limit of the imaging system. Despite efforts to filter out particles, the higher Re number flow contained some particles or droplets, which must be removed through image processing. Lastly, laser beam steering is exacerbated in the high Re flow, as shown by the stripes in the image. Routines were written in IDL to remove particles/droplets via edge-finding and linear interpolation. A sample of raw and processed images are shown below with a closeup showing the correction of a sample particle.

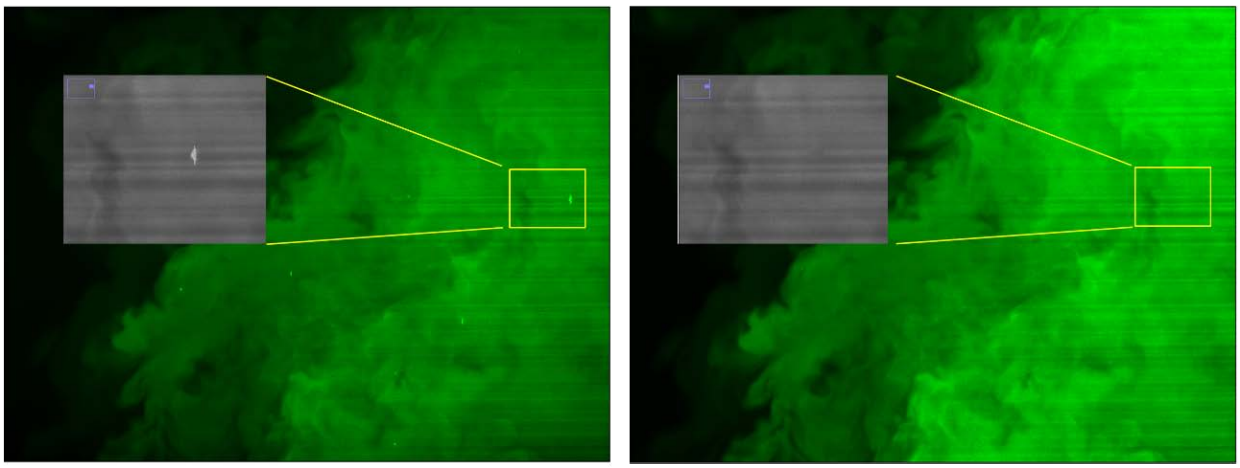

Fig. 20 Image processing for particle/droplet removal: raw (left) and processed (right)

Although the corrections worked well on the majority of the images, about 5% of the images could not be corrected and were discarded. Problems in the correction algorithm included the false identification of particles due to steep gradients in the signal from beam-steering and sharp transitions in mixture fraction. In addition, particles that did not have sharp edges but rather appeared as a "glow", were not identified.

The mixture fraction and scalar dissipation were calculated from the corrected Rayleigh scattering images. To investigate the distribution of dissipation with spatial frequency, we calculated the mean power spectral density (PSD) at each measurement location using 600 images. The spatial frequency corresponding to 2% of the peak power spectral density is a cutoff frequency above which there is less than a 2% contribution to the mean dissipation. A sample PSD is shown below with the cutoff frequency indicated. The PSD without noise suppression is displayed as the black line. At high spatial frequencies, the noise produces an apparent dissipation that overwhelms the measurement. However, interlacing can be used to suppress the noise and provide a good measurement of λ_c (red line). In the example below, λ_c is determined to be about 1.8 mm^{-1}, corresponding to structures about 500 µm in size.

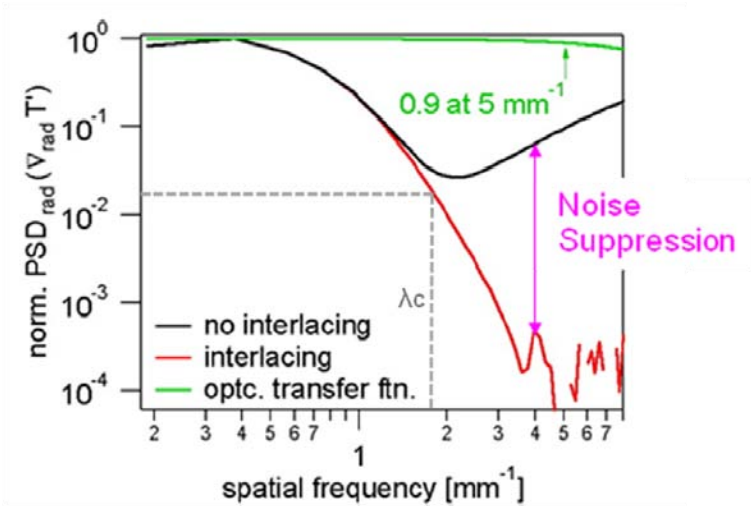

Fig. 21 Noise suppression through interlacing to determine the cutoff frequency, λ_c

Figure 22 shows the measured PSDs and values of λ_c at an axial position of x/d=20 for Re=22,000 and for Re=90,000. The different colors represent different radial positions from the jet centerline. At Re=22,000, the cutoff frequency was approximately 280 μm, and could be well resolved. In the higher Reynolds number flow, the dimensions of the fine-scale turbulent structures approach the resolution limit of the imaging system, and the cutoff frequency is located near the noise limit of the PSD. Scaling laws predicted that at Re = 90,000 the cutoff frequency should be on the order of 100 μm, and the measured cutoff frequency was approximately 120 μm. A detailed analysis of the Reynolds number dependence of the dissipation field is ongoing and results will be compared with LES simulations at Sandia.

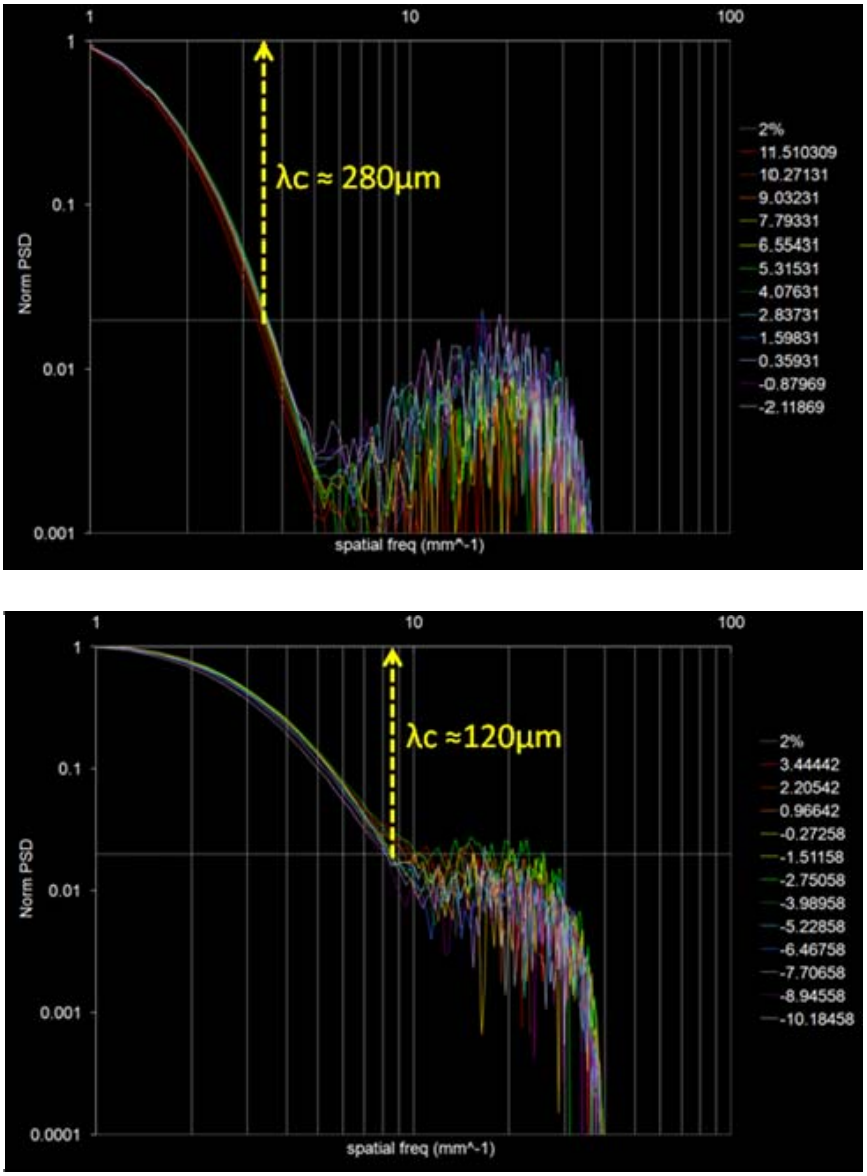

Fig. 22 Comparison of λ_c for Re=22,000 (top) and Re=90,000 (top)

5. SUMMARY OF ACCOMPLISHMENTS

At Texas A&M University, a set of tools has been developed to study non-thermochemical equilibrium (NTE) flows. Fundamental studies have laid the groundwork for future diagnostics on subsonic and hypersonic NTE flowfields. In addition, new laser diagnostic techniques for studying these types of flowfields have been demonstrated. However, these techniques are not limited to NTE flowfields and could be applied towards a variety of flowfields. The specific conclusions and recommendations from each of the major experiments are briefly summarized here.

A radio-frequency (RF) discharge was generated within a subsonic flowfield and characterized using broadband and narrowband emission spectroscopy, and CARS spectroscopy. The emission spectra concluded that the plasma imparted only slight gas heating (35 +/- 3 K) with negligible molecular dissociation. N_2 CARS pointwise measurements at several streamwise locations verified that the plasma induced vibrational excitation. The experimentally observed decay of the non-thermal equilibrium gases agreed well with predictions from vibrational kinetics modeling which included all relevant species in the flow. The model provided a good starting point against which future characterization of the RF plasma can be compared.

Software was written for processing NO PLIF images. NO PLIF is typically not employed at room temperature, and especially not for flows with small temperature variations. Since the temperature fluctuations imparted by the RF were expected to be small (300+/-35K), noise-reducing routines were examined and applied in a computer-based study. These studies concluded that Gaussian smoothing, dividing by a mean image, background subtraction, and selection of probed rotational lines, were all important for minimizing the noise and recovering true temperature variations while preserving spatial resolution. . Experimental implementation of recommendations from the computational study produced images with temperature uncertainties of <1.5%, or <5K at room temperature, proving that true temperature fluctuations expected from the RF plasma would be easily distinguishable.

New approaches to molecular tagging velocimetry (MTV) were investigated using NO LIF imaging. One of the main advantages of MTV techniques as opposed to particle-based techniques such as PIV lies in the ability of molecules to accurately track the flow, especially in the vicinity of strong shocks. First, single line MTV measurements were conducted utilizing photodissociation of NO_2. This study was demonstrated in the well-studied underexpanded jet flowfield, but could be extended towards a variety of other flowfields. Photodissociation of NO_2 at 355 nm produced a non-thermal equilibrium distribution of $NO_{v=1}$: $NO_{v=0}$ which corresponded to a vibrational temperature of about 7000K. A comparison of the MTV measurements using excitation of transitions in the A-X(1,1) and (0,0) bands of NO demonstrated significant advantages for the (1,1) transition. This advantage would be especially useful in a flowfield with naturally occurring NO such as a combustion flowfield, where most of the background NO would exist in the v=0 state.

The vibrational temperature evolution was explored and compared to vibrational kinetics modeling with good agreement. The primary mechanism for energy transfer was found to be vibrational quenching of $NO_{v=1}$ by O atoms formed through NO_2 photodissociation. We expect

that this model will be useful for validation against future experimental characterization of RF plasmas.

The single component MTV technique was extended to yield two components of velocity (streamwise and radial) in an underexpanded free jet through the use of a grid rather than a single line. Comparisons of two approaches to MTV measurements with NO showed that the NO fluorescence lifetime technique is advantageous in low quenching and high speed flows, while the photodissociation technique is preferable in high quenching and/or low speed flows. The photodissociation technique was not affected by quenching, and a much longer time delay could be used, since NO is a stable molecule and the persistence of the signal is essentially only limited by fluid mixing and diffusion or convection out of the probe laser sheet. The two-component technique produced velocity maps which agreed well with CFD simulations. Single shot analyses of the photodissociation technique yielded relative velocity uncertainties of ~5% and were limited by signal to noise ratios of the NO LIF measurements. This study demonstrates the first known application of either the NO fluorescence or NO_2 photodissociation techniques for two-component velocity mapping.

Both the single and two-component velocimetry methods gave low single-shot relative uncertainties (~5%), rendering them useful for short runtime facilities such as blowdown facilities and shock tubes, where runtimes may range anywhere from a few milliseconds to a few minutes, and/or for statistical measurements in dynamic flowfields. Both methods were dependent on good signal to noise, and resolution and uncertainties could be improved with increases in signal.

The compilation of all of the above topics represents a collection of diagnostic tools that may be used to characterize and understand not only NTE systems, but can be extended for use in a variety of flowfields.

Lastly, research at Sandia's CRF demonstrated quench-free NO PLIF measurements using a picosecond pulsed laser for excitation and a fast-gated intensified camera for detection. In addition, laser Rayleigh scattering measurements were performed to measure the fine-scale turbulent structures in turbulent non-reacting jets. Results of the turbulent jet measurements are currently being compared to large-eddy simulations by Joe Oefelein at Sandia.

6. References

Atkinson, R., Baulch, D., Cox, R., Crowley, J., Hampson, R., Hynes, R., Jenkin, M., Rossi, M., Troe, J., "Evaluated Kinetic and Photochemical Data for Atmospheric Chemistry: Volume I - Gas Phase Reactions of Ox, HOx, NOx and SOx Species," *Atmospheric Chemistry and Physics*, Vol. 4, 2004, pp. 1461-1738.

Bass, H., "Absorption of Sound by Air: High Temperature Predictions," *Journal of Acoustic Society of America*, Vol. 69, No. 1, 1981, pp. 124-138.

Bauer, S., Caballero, J., Curtis, R., Wiesenfeld, J., "Vibrational Relaxation Rates of CO_2(001) with Various Collision Partners for T<300K," *Journal of Physical Chemistry*, Vol. 91, No. 7, 1987, pp. 1778-1785.

Bowersox, R., North, S., Srinivasan, R., "High-Speed Free Shear Layers with Molecular Non-Equilibrium: An Example of the Fluids Information Triad (Invited)," *46th AIAA Aerospace Sciences Meeting and Exhibit*, AIAA-2008-0685, Reno, Nevada, 2008.

Breen, J., Quy, R., Glass, G., "Vibrational Relaxation of O_2 in the Presence of Atomic Oxygen," *Journal of Chemical Physics*, Vol. 59, No. 1, 1973, pp. 556-557.

Brooks, C., Hancock, G., Saunders, M., "Dependence of the Nascent Vibrational Distribution of NO(v) on the Photolysis Wavelength of NO_2 in the Range λ=266-327 nm Measured by Time-resolved Fourier Transform Infrared Emission," *Physical Chemistry Chemical Physics*, Vol. 9, 2007, pp. 5232-5240.

Candler, G., Kelley, J., Macheret, S., Shneider, M., Adamovich, R., "Vibrational Excitation, Thermal Nonuniformities, and Unsteady Effects on Supersonic Blunt Bodies," *AIAA Journal*, Vol 40, No. 9, 2002, pp. 1803-1810.

Cannemeyer, F., Vries, A., "Vibrational Relaxation of CO_2 in CO_2-N_2 and CO_2-O_2 Mixtures," *Physica*, Vol. 74, 1974, pp. 196-204.

Castle, K., Hwang, E., Dodd, J., "Laboratory Studies of CO_2(v_2)-O Vibrational Energy Transfer," *Proceedings of SPIE*, Vol. 5235, Bellingham, WA, 2004

Cramp, J., Lambert, J., "Vibrational Relaxation of CO_2(v_3) by O Atoms," *Chemical Physics Letters*, Vol. 22, No. 1, 1973, pp. 146-149.

Demore, W., Sander, S., Golden, D., Hampson, R., Kurylo, J., Howard, C., Ravishankara, A., Kolb, C., Molina, J., "Chemical Kinetics and Photochemical Data for Use in Stratospheric Modeling," *JPL Publication 97-4*, 1997, pp. 1-266.

Dodd, J., Lockwood, R., Hwang, E., Miller, S., Lipson, S., "Vibrational Relaxation of NO(v=1) by Oxygen Atoms," *Journal of Chemical Physics*, Vol. 11, No. 8, 1999, pp. 3496-3507.

Donaldson, C. D., Snedeker R. S., "A Study of Free Jet Impingement. Part 1. Mean Properties of Free and Impinging Jets," *Journal of Fluid Mechanics*, Vol. 45, Part 2, 1971, pp. 281-319.

Finzi, J., Hovis, F., Panfilov, V., Hess, P., Moore, C., "Vibrational Relaxation of Water Vapor," *Journal of Chemical Physics*, Vol. 67, No. 9, 1977, pp. 4053-4961.

Harrison, J., Yang, X., Rosslein, M., Felder, P., Huber, J., "Photodissociation of NO_2 at 355 and 351 nm Investigated by Photofragment Translational Spectroscopy," *Journal of Physical Chemistry*, Vol. 98, 1994, pp. 12260-12269.

Huetz-Aubert, M., Tripodi, R., "Rate Equations for the Vibrational Relaxation of CO_2-N_2 or CO_2-Noble Gas Mixtures- Application to Comparison of Spectrophone Data with Results from Other Experimental Techniques," *Journal of Chemical Physics*, Vol. 55, No. 12, 1971, pp. 5724-5734.

Hunter, M., Reid, S. A., Robie, D. C., Reisler, H., "The Monoenergetic Unimolecular Reaction of Expansion-Cooled NO_2: NO Product State Distributions at Excess Energies 0-3000cm^{-1}," *Journal of Chemical Physics*, Vol. 99, No. 2, 1993, pp. 1093-1108.

Ianni, J., KINTECUS, Windows XP Version, www. Kintecus.com, 2008.

Ismailov, M. M., Schock H. J., Fedewa, A. M., "Gaseous Flow Measurements in an Internal Combustion Engine Assembly Using Molecular Tagging Velocimetry," *Experiments in Fluids*, Vol. 41, 2006, pp. 57-66.

Joly, V., Marmignon, C., "Effect of H_2O Vapor on the Vibrational Relaxation in Hypersonic Wind Tunnels," *Journal of Thermophysics and Heat Transfer*, Vol. 11, No. 2, 1977, pp. 266-272.

Kosanetzky, J., List, U., Urban, W., Vormann, H., "Vibrational Relaxation of NO($X_2\Pi$,v=1) Studied by an IR-UV-Double-Resonance Technique", *Chemical Physics*, Vol. 50, 1980, pp 361-371.

Lee, M., McMillin, B., Hanson, R., "Temperature Measurements in Gases by Use of Planar Laser-Induced Fluorescence Imaging of NO," *Applied Optics*, Vol. 32, No. 27, 1993, pp 5379-5396.

Lucht, R., Velur-Natarajan, V., Carter, C., Grinstead, K., Gord, J., Danehy, P., Fiechtner, G., Farrow, R., "Dual-Pump Coherent Anti-Stokes Raman Scattering Temperature and CO_2 Concentration Measurements," *AIAA Journal*, Vol. 41, No. 4, 2003, pp. 679-686.

Lucht, R., "Three-Laser Coherent Anti-Stokes Raman Scattering Measurements of Two Species," *Optics Letters*, Vol. 12, 1987, pp. 78-80.

Luque, J., Crosley, D. R., "LIFBASE: Database and Spectral Simulation Program (Version 1.5)," SRI International Report MP 99-009, 1999.McNeal, R., Whitson, M., Cook, G., "Quenching of

Vibrationally Excited N_2 by Atomic Oxygen," *Chemical Physics Letters*, Vol. 16, No. 13, 1972, pp. 507-510.

Palmer, J., Hanson, R., "Planar Laser-Induced Fluorescence Imaging in Free jet Flows with Vibrational Nonequilibrium," *31st AIAA Aerospace Sciences Meeting and Exhibit*, AIAA-93-0046, Reno, Nevada, 1993.

Palmer, J., Hanson, R., "Single-Shot Velocity Using Planar Laser-Induced Fluorescence Imaging of Nitric Oxide," *29th Joint Propulsion Conference and Exhibit*, AIAA-93-2020, Monterey, California, 1993.

Palmer, R., "The CARSFIT Computer Code for Calculating Coherent Anti-Stokes Raman Spectra: User and Programmer Information," Sandia Report SAND89–8206: Sandia National Laboratories, Livermore, CA., 1989.

Ree, J., "Theoretical Investigation of the Vibrational Relaxation of Nitric Oxide (n=1-7) in Collisions with Oxygen and Nitrogen," *Bulletin of the Korean Chemical Society*, Vol. 14, No. 1, 1993, pp. 47-52.

Ribarov, L. A., Wehrmeyer, J. A., Hu, S., Pitz, R.W., "Multiline Hydroxyl Tagging Velocimetry Measurements in Reacting and Nonreacting Experimental Flows," *Experiments in Fluids*, Vol. 37, 2004, pp. 65-74.

Scalabrin, L., Boyd, I., "Development of an Unstructured Navier-Stokes Solver for Hypersonic Nonequilibrium Aerothermodynamics," *38th AIAA Thermophysics Conference*, AIAA 2005-5203, Toronto, Canada, 2005.

Stephenson, J., "Vibrational Relaxation of NO($X_2\Pi$,v=1) in the Temperature Range 100-300K," *Journal of Chemical Physics*, Vol. 60, No. 11, 1974, pp. 4289-4294.

Stier, B., Koochesfahani, M., "Molecular Tagging Velocimetry (MTV) Measurements in Gas Phase Flows," *Experiments in Fluids*, Vol. 26, 1999, pp. 297-304.

Tsang, W., Hampson, R., "Chemical Kinetic Data Base for Combustion Chemistry. Part I. Methane and Related Compounds," *Journal of Physics Chemistry Reference Data*, Vol. 15, No.3, 1986, pp. 1087-1222.

Woodmansee, M. A., Iyer, V., Dutton, J. C., Lucht, R. P., "Nonintrusive Pressure and Temperature Measurements in an Underexpanded Sonic Jet Flowfield," *AIAA Journal*, Vol. 42, No. 6, 2004, pp. 1170-1180.

Zuckerwar, A., Miller, K., "Vibrational-Vibrational Coupling in Air at Low Humidities," *Journal of Acoustic Society of America*, Vol. 84, No. 3, 1988, pp. 970-977.

DISTRIBUTION

1 Simon W. North
Department of Chemistry
Texas A&M University
PO BOX 3012
Corner of Ross and Spence Street
College Station, TX 77840

2 Rodney Bowersox
Department of Aerospace Engineering
Texas A&M University
3141 TAMU
College Station, TX 77843-3141

3 Lawrence Livermore National Laboratory
Attn: N. Dunipace (1)
P.O. Box 808, MS L-795
Livermore, CA 94551-0808

4	MS9051	Jonathan Frank	8351
5	MS9018	Central Technical Files	8944
6	MS0899	Technical Library	9536
7	MS0123	D. Chavez, LDRD Office	1011


Sandia National Laboratories